molecules

MDPI

Article

Model Approach to Thermal Conductivity in Hybrid Graphene–Polymer Nanocomposites

Andriy B. Nadtochiy [1], Alla M. Gorb [1], Borys M. Gorelov [2], Oleksiy I. Polovina [1], Oleg Korotchenkov [1,3] and Viktor Schlosser [4,*]

[1] Faculty of Physics, Taras Shevchenko National University of Kyiv, 01601 Kyiv, Ukraine; nadtku@univ.kiev.ua (A.B.N.); alla.gorb@knu.ua (A.M.G.); fantality@ukr.net (O.I.P.); olegkorotchenkov@knu.ua (O.K.)
[2] Chuiko Institute of Surface Chemistry, NAS of Ukraine, 17 General Naumov Str., 03164 Kyiv, Ukraine; bgorel@ukr.net
[3] Erwin Schrödinger International Institute for Mathematics and Physics, University of Vienna, 1090 Vienna, Austria
[4] Department of Electronic Properties of Materials, Faculty of Physics, University of Vienna, 1090 Wien, Austria
* Correspondence: viktor.schlosser@univie.ac.at; Tel.: +43-1-4277-72611

Abstract: The thermal conductivity of epoxy nanocomposites filled with self-assembled hybrid nanoparticles composed of multilayered graphene nanoplatelets and anatase nanoparticles was described using an analytical model based on the effective medium approximation with a reasonable amount of input data. The proposed effective thickness approach allowed for the simplification of the thermal conductivity simulations in hybrid graphene@anatase TiO_2 nanosheets by including the phenomenological thermal boundary resistance. The sensitivity of the modeled thermal conductivity to the geometrical and material parameters of filling particles and the host polymer matrix, filler's mass concentration, self-assembling degree, and Kapitza thermal boundary resistances at emerging interfaces was numerically evaluated. A fair agreement of the calculated and measured room-temperature thermal conductivity was obtained.

Keywords: multilayer graphene; anatase; epoxy; polymer nanocomposites; thermal conductivity; Kapitza thermal boundary resistance

check for updates

Citation: Nadtochiy, A.B.; Gorb, A.M.; Gorelov, B.M.; Polovina, O.I.; Korotchenkov, O.; Schlosser, V. Model Approach to Thermal Conductivity in Hybrid Graphene–Polymer Nanocomposites. *Molecules* **2023**, *28*, 7343. https://doi.org/10.3390/molecules28217343

Academic Editor: Victor M. García-Suárez

Received: 5 September 2023
Revised: 24 October 2023
Accepted: 26 October 2023
Published: 30 October 2023

Copyright: © 2023 by the authors. Licensee MDPI, Basel, Switzerland. This article is an open access article distributed under the terms and conditions of the Creative Commons Attribution (CC BY) license (https://creativecommons.org/licenses/by/4.0/).

1. Introduction

Polymer nanocomposites based on graphene and its derivatives remain the focus of numerous theoretical and experimental multidisciplinary types of research, which describe some novel structural [1–4], mechanical [5–7], electrical [8–10], and thermal [11–14] properties of the composites.

Such attention to the nanocomposites is fed by their promise as high-efficiency materials in a very wide range of applications. These include, for example, thermal interface materials [15–17], active electrodes for energy storage devices such as Li-ion batteries [18–20] and supercapacitors [21–23], membranes for fuel cells [24–28], gas sensors [29,30], and electromagnetic shields [31–33].

The state-of-the-art investigation of polymer nanocomposites has advanced over the past decade and generated several comprehensive review articles [34–41]. The key questions raised are how the filler content impacts the overall properties of the composite and to what extent the polymer–graphene interphase interaction variations, both with the morphology and surface activity of the filler, can be accounted for.

Recently, polymeric nanocomposites based on graphene/metal oxide hybrid nanostructures have been studied intensively as promising materials for the various above-mentioned applications [23,42–49]. A great variety of nano-sized metal oxides have been

tested as anchoring layers on graphene and graphene oxide nanoplatelets, graphene-wrapped or graphene-encapsulated hybrid particles for fabricating advanced composite electrode materials for lithium-ion batteries [42,43], and electrochemical capacitors [23,42]. Examples of oxides include (but are not limited to) simple oxides (Cu_2O, MnO, NiO, ZnO, CuO, SnO_2, CeO_2, RuO_2, TiO_2, MoO_2, MnO_2, Fe_2O_3, Fe_3O_4, Mn_3O_4, Co_3O_4, V_2O_5, and MoO_3) and complex oxides ($LiFePO_4$, $Li_3V_2(PO_4)_3$, and $Li_4Ti_5O_{12}$).

Among the other oxides employed in hybrid graphene/metal oxide and graphene oxide/metal oxide fillers, a unique place pertains to two well-known allotropies of titanium dioxide (TiO_2), namely rutile and anatase. Today, graphene@TiO_2- and graphene oxide@TiO_2-based polymer nanocomposites are promising materials that are not only used in energy storage applications but also in photocatalysis [44,45], gas sensing [46], solar cells [47], water splitting [48], and proton exchange membranes [49]. Great attention has been paid to graphene@TiO_2 and graphene oxide@TiO_2 hybrid nanoparticles because titanium dioxide nanoparticles demonstrate nontoxicity and good compatibility with organic solvents and polymers, and they also display good hydrophilicity and mechanical and thermal stabilities [50–52]. Also, the particular surface defect structure of titanium dioxide [53,54] endows it with highly reactive surface sites, which influence the interfacial charge and phonon transfer kinetics in composites with embedded TiO_2 [55,56]. Following the comments of Wu et al. [42], the functions and synergistic effects of graphene/metal oxide hybrid nanoparticles embedded into a polymer matrix, which are related to the composite's transport properties, can be briefly summarized as follows:

(1) Graphene nanoplatelets play the roles of 2D supports to uniformly anchor or disperse metal oxides with well-defined sizes, shapes, and crystallinity;

(2) Graphene nanoplatelets act as 2D conductive templates to build a 3D conductive porous network to improve the poor electrical properties and charge transfer pathways of pure oxides;

(3) Graphene nanoplatelets suppress the volume change and agglomeration of metal oxide nanoparticles;

(4) Metal oxide nanoparticles suppress the re-stacking of individual graphene nanoplatelets;

(5) Metal oxide nanoparticles can promote both charge and phonon out-of-plane transfer in multilayered graphene (MLG) nanoplatelets by binding dangling edge carbon bonds of neighboring monoatomic layers with the active sites located on the metal oxide nanoparticles.

Typically, the synthesis of MLG-TiO_2 nanocomposites includes in situ growth and covalent and non-covalent grafting [57]. One should bear in mind that the rational design of hybrid nanoparticle architecture and the control of the morphology and phase composition of metal oxides on graphene can ensure reproducibility and a better understanding of the structure–property relationships in the nanocomposites. Also, a clear perception of the surface chemistry on graphene and metal oxides is crucial for the enhancement of the interfacial synergistic effects that are favorable for improved phonon transport.

The thermal conductivity of the composites is restricted by the high thermal interfacial resistance originating from strong interfacial phonon scattering. To obtain a thermal interface material with nanocomposites containing high thermal conductivity fillers, their concentration would thus be rather high. However, as the material is expected to be electrically insulating to prevent the malfunction of electronic devices at high working voltages, this requires low filler concentrations. Most frequently, reasonable thermal conductivities in the nanocomposites will inevitably result in enhanced electrical conductivities due to a low percolation threshold. Meanwhile, an increased thermal conductivity with filler loading and simultaneously decreased electrical conductivity were reported to arise from the attachment of functionalized molecules or nanoparticles to the filler surface [58,59].

Assuming that the temperature field obeys a diffusive equation, the kinetic theory predicts the Fourier law to be $q = -\kappa\Delta T$ with the heat flux q, thermal conductivity κ, and temperature gradient ΔT. In solids, heat is carried by acoustic phonons and electrons so that the thermal conductivity can be represented as a two-term sum, $\kappa = \kappa_{ph} + \kappa_e$,

with phonon (κ_{ph}) and electron (κ_e) contributions. In metals, κ_e dominates due to a large concentration of free carriers (κ ~380–400 W/m K in copper). In insulating crystals, heat is transported via lattice vibrations, and the Boltzmann–Peierls approach [60] became one of the cornerstones in the theory of lattice thermal conductivity κ_{ph}.

It is, however, generally agreed that heat conduction in carbon materials is usually dominated by phonons, even in graphite, which has metal-like properties [61]. This is readily explained by the strong covalent sp^2 bonding and resulting efficient heat transfer via lattice vibrations, an assertion for which there is prior evidence. However, it is likely that the contribution of κ_e will be significant for the doped materials [62].

In the relaxation time (τ) approximation, various scattering mechanisms, which limit the phonon mean free path ($\Lambda = \tau v$, with v being the phonon group velocity, which is approximated by the sound velocity when the acoustic dispersion can be ignored), are additive for the i-th scattering processes, so that $\tau^{-1} = \sum_i \tau_i^{-1}$. The acoustic phonons are scattered by other phonons, lattice defects, impurities, free electrons, interfaces, etc.

The most elementary picture of heat conductivity is based on the analogy with the kinetic theory of gases when $\kappa_{ph} = \frac{1}{3} C_p v \Lambda$, where C_p is the specific heat capacity. In a lattice, the oscillating particles are replaced with normal vibration modes, which possess well-defined wavelengths and frequencies. It is also necessary to take into account that the different modes obey different dispersion relations and thus have different group velocities v_j depending on their wavenumber (or frequency). One can thus equate $\kappa_{ph} = \sum_j C_j(\omega) v_j^2(\omega) \tau_j(\omega) d\omega$, where C_j is the heat capacity, and ω is the phonon frequency, and the summation extends over all j phonon polarization branches (two transverse and one longitudinal acoustic branch).

Thermal conductivity is called intrinsic when it is limited by the crystal lattice anharmonicity. The intrinsic κ limit is reached when the crystal lattice is perfect, and phonons can only be scattered by other phonons. The anharmonic phonon interactions, which lead to finite κ in three dimensions, can be described by the Umklapp processes. The degree of the anharmonic interatomic forces is characterized by the Grüneisen parameter γ, which enters the expressions for the Umklapp scattering rates. Thermal conductivity is termed extrinsic when it is mostly limited by extrinsic effects, such as phonon scattering on rough boundaries or lattice defects [62]. In epoxy–carbon composites, the electronic thermal conductivity is less than 2% of the thermal conductivity of the material and, therefore, may be considered negligible [63].

In nanostructures, κ is reduced by scattering from boundaries. Specular scattering with momentum conservation does not add to thermal resistance. Only diffuse phonon scattering from rough interfaces without momentum conservation ($p \rightarrow 0$) limits the free path Λ.

If the boundary scattering dominates, $\kappa_{ph} \sim C_p v \Lambda \sim C_p v^2 \tau_B \sim C_p v D$. At $D \ll \Lambda$, phonon dispersion is modified due to confinement, resulting in a changing v value and complicating the size dependence of κ_{ph} [62]. C_p is determined by the phonon densities of states, which are effectively modified by reducing the dimensionality. Consequently, $\kappa_{ph} \sim T^3$ is obtained at low temperatures in bulk materials and $\kappa_{ph} \sim T^2$ is seen in 2D systems.

It is unlikely, however, that the above equations can be easily generalized to the case of heterogeneous composites, such as polymer–graphene composites. Despite the long-standing interest in the development of a suitable model describing the heat transfer through the matrix–filler interphase, models of the thermal conductivity in such systems remains highly controversial [59]. Our understanding of the heat transport phenomena is even more rudimentary for functionalized fillers such as graphene/metal oxide fillers.

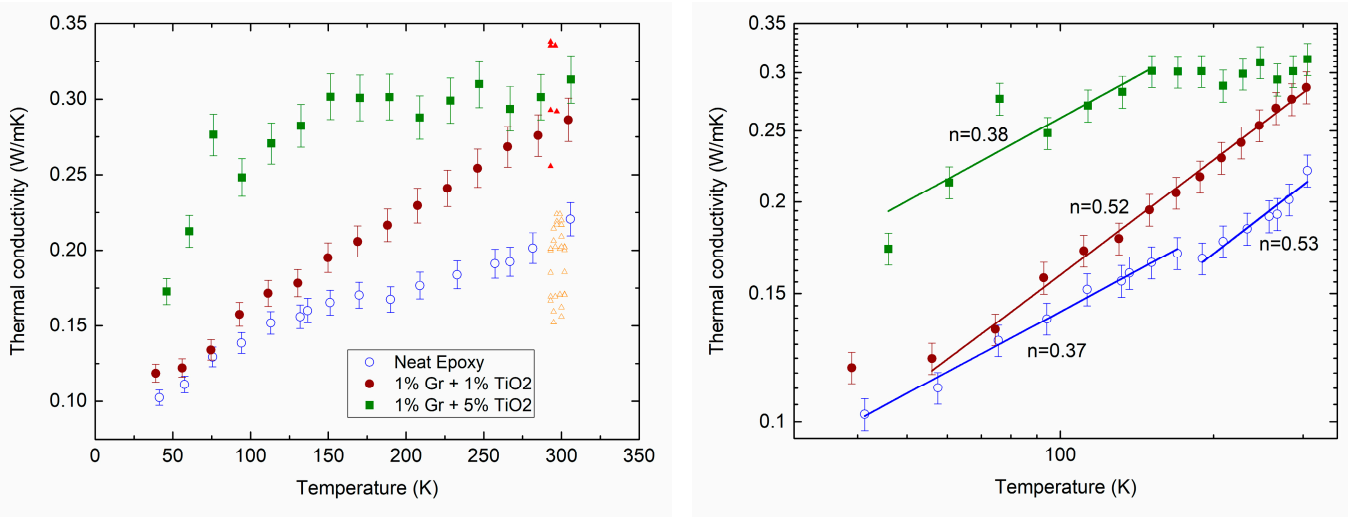
Here, we prepared epoxy nanocomposites with MLG and embedded nanoparticles of TiO_2 and studied a temperature dependence of the thermal conductivity of the material in the range from about 40 to 300 K. The thermal conductivity of the composite was numerically computed as a function of the two-layer filler loading. The proposed soft-sphere approach and related concept of the effective thickness allowed us to simplify the

thermal conductivity simulations by replacing a dotty interface with a continuous one and by describing interface thermal transport in the hybrid graphene@anatase TiO_2 nanosheets via the phenomenological thermal boundary resistance.

2. Results and Discussion

2.1. Temperature Dependence of the Thermal Conductivity

Figure 1a shows the measured temperature dependencies of the thermal conductivity of the neat epoxy (open circles) and its composites filled with hybrid MLG@TiO_2 nanoparticles with different filler contents, C_{f1}:C_{f2} = 0.01:0.01 (closed circles) and 0.01:0.05 (squares). The experimental data show aggregate behaviors that are typical of the thermal conductivity in disordered materials. Indeed, we previously reviewed extensive studies on amorphous oxides [64].



(**a**) (**b**)

Figure 1. Measured temperature dependencies of κ for the neat epoxy (open circles) and epoxy-MLG@TiO_2 nanocomposites with different mass loading ratios for MLG (C_{f1}) and TiO_2 (C_{f2}): C_{f1} : C_{f2} = 0.01:0.01 (closed circles) and 0.01:0.05 (squares) on lin–lin (**a**) and log–log (**b**) scales. Lines in (**b**) are fitted to a power law $\kappa(T) \propto T^n$ with the exponent values n. Triangles in (**a**) are the calculated results at 300 K (for a detailed description, see Section 2.5). They are arbitrarily shifted along the temperature axis for better comparison.

As an example, the computed $\kappa(T)$ behavior in amorphous SiO_2 (a-SiO_2) is depicted in Figure 2. The $\kappa(T)$ dependence can be described by calculating the total mean free path Λ as a combination of various phonon scattering mechanisms using the Matthiessen rule,

$$\frac{1}{\Lambda} = \sum_i \frac{1}{\Lambda_i}, \quad (1)$$

where the sum runs over all scattering mechanisms, e.g., phonon–phonon, phonon–boundary, phonon–point defect scattering, etc.

In disordered materials, the glass-like $\kappa(T)$ dependence is characterized by the initial $\kappa \sim T^2$ rise at very low temperatures, followed by a characteristic plateau around 10 K (marked by arrow S in Figure 2) and a further slow increase, which is weaker than $\kappa \sim T^2$, with the increasing temperature [66]. Such $\kappa(T)$ dependence is exemplified in Figure 2.

The physical mechanisms that may be responsible for such behavior have been extensively debated. The T^2 dependence at the lowest T has been shown to be well described by the scattering on statistically distributed localized tunneling entities [67,68]. The plateau and gradually increasing κ at higher temperatures are well described by incorporating the soft-potential model [69,70].

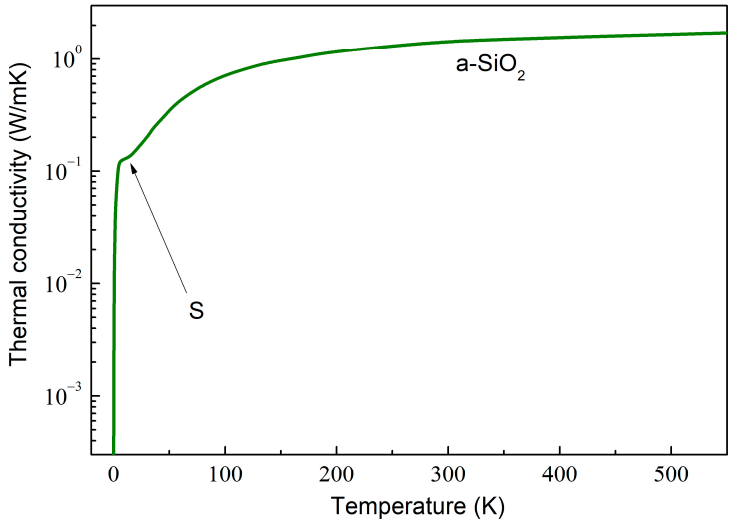


Figure 2. A log–lin plot of the thermal conductivity of amorphous SiO_2, calculated by using the data obtained by Goodson et al. [65].

The gradual increase in the thermal conductivity shown by the circles in Figure 1 is hence in qualitative agreement with the above prediction. The $\kappa(T)$ dependence given by the squares is observed to saturate above $\approx$ 150 K. A small plateau can also be seen between 150 and 200 K for the net epoxy (open circles). The inclusion of MLG@TiO_2 nanoparticles increases the thermal conductivity (closed circles in Figure 1). Increasing the concentration of TiO_2 shows a further enhancement in κ (squares compared with closed circles in Figure 1). It is not immediately obvious how the above models can be combined for the interpretation of the experimental results.

2.2. Development of the Model Formalism

In constructing a suitable model to describe the experimental data, we begin by picking the thermal conductivities of epoxy, graphene, and anatase TiO_2 along with the thermal boundary resistances, which are given in Table 1.

Table 1. Physical parameters of the constituent phases.

Material	Density, ρ (kg m^{-3})	Thermal Conductivity, κ (W m^{-1} K^{-1})	Kapitza Thermal Boundary Resistance, r_n (W^{-1} m^2 K)
epoxy	1.200×10^3 [71]	0.22 (our data)	–
graphene	2.267×10^3 [72]	in-plane $\kappa_{g\parallel}$ = 600–1200 cross-plane $\kappa_{g\perp}$ = = 6 [73]	–
anatase TiO_2	3.88×10^3 [74]	0.455 [75]	–
graphene–epoxy interphase	–	–	3.5×10^{-9} [76]
anatase–epoxy interphase	–	–	$(0.1-1.0) \times 10^{-8}$ [77,78]
graphene–anatase interphase	–	–	*

* There are no data available in the literature.

It should be noted that the theoretical calculations based on Maxwell Garnett's effective media approximation [75] showed that, at low loadings ($\varphi_{f1} \leq 2\%$), the thermal conductivity does not depend on the graphene–epoxy thermal boundary resistance (r_1) when it varies in the range from $0.35 \times 10^{-8} \leq r_1 \leq 8.3 \times 10^{-8}$ m^2·K·W^{-1} (see Figure 4b in ref. [76]).

It has been widely observed that the introduction of the Kapitza thermal boundary resistance between the MLG nanoplatelets and a host polymer matrix into the model

can provide readable accounts of the thermal conductivity experiments and theoretical approaches. In hindsight, the heat transfer enhancement in nanocomposites is largely determined by the thermal boundary resistance, but the conventional heat conduction models for the interfaces fail to have the correct value of the thermal boundary resistance.

We begin with the development of our model by introducing the Kapitza resistance [79] R_K between the thermally conductive filler nanoparticle with the thermal conductivity κ_f and the 3D polymer matrix (κ_m), which arises from the large difference in the phonon density of states of the low-dimensional and bulk media. The Kapitza resistance is in series with the particle thermal resistance $\updownarrow_f/\kappa_f$, where $\updownarrow_f$ is the filler particle size [77]. For simplicity, let us consider the equivalent thermal resistance as $\left(\frac{\updownarrow_f}{\kappa_f}\right)_{eff} = \frac{\updownarrow_f}{\kappa_f} + R_K$ and assume that the effective thermal conductivity of the particle is [77]

$$\kappa_{f,eff} = \frac{\kappa_f}{1 + \frac{R_K \kappa_f}{\updownarrow_f}} = \frac{\kappa_f}{1 + \frac{\eta_f}{\updownarrow_f}}, \quad (2)$$

where η_f is the Kapitza length. This can be introduced to describe the length scale, which is defined by the equality of the interface thermal resistance to the heat flux and the thermal resistance originating from the bulk [80]. The existence of the thermal boundary resistance leads to a temperature drop $\Delta\theta$ across the interface and [80]

$$R_K = \frac{\Delta\theta}{Q_i} = \frac{\eta_{m,f}}{\kappa_{m,f}}, \quad (3)$$

where Q_i is the heat flux across the interface, whereas the subscripts m and f indicate the matrix and filler, respectively. The most widely accepted case for removing R_K from the thermal conductivity expression is extending the problem to a large-scale system, when the interface thermal resistance can usually be neglected. By increasing the interparticle separation distance and filler size $\updownarrow_f$ a smaller portion of $\left(\frac{\updownarrow_f}{\kappa_f}\right)_{eff}$ is related to the interface.

Here, we approximate hybrid MLG@TiO_2 nanoparticles using the two bounding surfaces denoted by the subscripts 1 (MLG) and 2 (TiO_2) so that

$$\frac{\updownarrow_{f1} + \updownarrow_{f2}}{\kappa_{h,eff}} = \frac{\updownarrow_{f1}}{\kappa_{f1}} + R_{K1} + \frac{\updownarrow_{f2}}{\kappa_{f2}} + R_{K2} = \frac{\updownarrow_{f1}\kappa_{f2} + \updownarrow_{f2}\kappa_{f1} + (R_{K1} + R_{K2})\kappa_{f1}\kappa_{f2}}{\kappa_{f1}\kappa_{f2}}, \quad (4)$$

where R_{K1} and R_{K2} stand for the MLG-TiO_2 and TiO_2-epoxy interfaces, respectively. The effective thermal conductivity of the hybrid nanoparticle ($\kappa_{h,eff}$) is then readily obtained as

$$\kappa_{h,eff} = \frac{\kappa_{f1}}{\frac{\updownarrow_{f1}}{\updownarrow_{f1}+\updownarrow_{f2}} \cdot \left(1 + \frac{\eta_{f1}}{\updownarrow_{f1}}\right) + \frac{\updownarrow_{f2}}{\updownarrow_{f1}+\updownarrow_{f2}} \cdot \left(1 + \frac{\eta_{f2}}{\updownarrow_{f2}}\right) \cdot \frac{\kappa_{f1}}{\kappa_{f2}}}. \quad (5)$$

However, the above approach implies the existence of a distinct boundary between the constituent phases. Moreover, there are no contributions in Equations (2)–(5) to account for the geometrical shape of the filling particles. Therefore, to account for the interphase layers surrounding the fillers of different shapes, the thermal conductivity of the interphase regions (κ_{int}) was determined using the Kapitza thermal boundary resistance R_K as [12]

$$\kappa_{int} = \frac{1}{h_{int}} \int_0^{h_{int}} \frac{h \cdot dh}{R_K} = \frac{h_{int}}{2R_K}, \quad (6)$$

where h_{int} is the interphase layer thickness. It should be noted that, since the interphase layers are composed of segments of macromolecular chains, the values of κ_{int} are supposed to be close to κ_m. It is therefore possible to roughly estimate a spread of the h_{int} values provided that the corresponding R_K value is known (or vice versa).

Using Equation (6), the above $\kappa_{f,eff}$ can be modified (see Supplementary Note S1). A graphical data analysis of both $\kappa_{f,eff}$ and $\kappa_{h,eff}$ at varying interphase layer parameters is performed in Section 2.5. The numerical estimates of η_f and the normalized effective thermal conductivities $\kappa_{f,eff}/\kappa_f$ are given in Table 2 for the anatase, the in-plane ($\kappa_{g11} = \kappa_{g22}$) and cross-plane ($\kappa_{g33}$) thermal conductivities of the MLGs, and the hybrid particles of the sandwich-like MLG@TiO_2 and of the graphene-wrapped anatase architectures. In the evaluation of κ_{int}, the value of 10 nm was taken for h_{int} (see comments in Section 2.5).

Table 2. Parameters of the epoxy/MLG@TiO_2 composite at 300 K, numerically simulated using Equations (2)–(6).

Interface	κ_f (W m^{-1} K^{-1})	R_K (m^2·K·W^{-1})	$\kappa_{int}=\frac{h_{int}}{2R_K}$ (W m^{-1} K^{-1})	$\updownarrow_f$ (nm)	$\eta_f=\kappa_f R_K$ (nm)	$\kappa_{f1,eff}/\kappa_{f1}$, $\kappa_{f2,eff}/\kappa_{f2}$, $\kappa_{h,eff}/\kappa_{f1}$ (W^{-1} m^2 K)
Anatase–epoxy	$\kappa_{f2} = 0.455$	$R_K = r_2 = 1.0 \times 10^{-8}$ (1.0×10^{-9})	1.2 (12.0)	$\updownarrow_{f2} = D = 50$	4.55 (4.55×10^{-1})	0.9166 (0.9910)
Graphene (in-plane)–epoxy	$\kappa_{f1} = \kappa_{g11} = \kappa_{g22} = 600.0$ (1200)	$R_K = r_1 = 3.5 \times 10^{-9}$	3.43 (3.43)	$\updownarrow_{f1} = L_x = L_y = 5 \times 10^3$	2.1×10^3 (4.2×10^3)	0.7042 (0.5435)
Graphene (cross-plane)–epoxy	$\kappa_{f1} = \kappa_{g33} = 6.0$	$R_K = r_1 = 3.5 \times 10^{-9}$	3.43	$\updownarrow_{f1} = L_z$ =50	2.1×10^1	0.7042
The sandwich-like MLG@TiO_2 structure						
Graphene (in-plane)–anatase–epoxy	600.0@0.455	$R_K = r_{2,1} = 1.0 \times 10^{-6}$ (1.0×10^{-7})		$L_x + \updownarrow_{f2}$	6.0×10^5 (6.0×10^4)	0.00746/0.00752 * (0.0369/0.0384) *
Graphene (cross-plane)–anatase–epoxy	6.0@0.455	$R_K = r_{2,1} = 1.0 \times 10^{-6}$ (1.0×10^{-7})		$L_z + \updownarrow_{f2}$	6.0×10^3 ** (6.0×10^2) **	0.01477/0.01489 * (0.0730/0.0760) *
Graphene-wrapped anatase						
Graphene-wrapped anatase–epoxy	606.0@0.455	$R_K = r_{2,1} = 1.0 \times 10^{-6}$ (1.0×10^{-7})		$2L_z + \updownarrow_{f2}$	6.0×10^3 ** (6.0×10^2) **	0.00022 (0.00116)

The values of κ_{int} were estimated by inputting $h_{int} = 24$ nm. * The nominator (denominator) corresponds to $r_2 = 1.0 \times 10^{-8}$ m^2·K·W^{-1} (1.0×10^{-9} m^2·K·W^{-1}). ** In the limit of $\updownarrow_{f2} \longrightarrow \infty$.

2.3. Discussing the Temperature Dependence of the Thermal Conductivity in Nanocomposites

We fitted the measured $\kappa(T)$ data to a power-law dependence $\kappa(T) \propto T^n$. The applied analysis yields several temperature regions of such dependence with the marked exponent values of n, as given by the lines in Figure 1b.

For the epoxy resins, a linear temperature dependence $\kappa(T) \propto T$ was observed in the region from 10 to 300 K [81,82]. In our neat epoxy, n varies from about 0.4 to 0.5 upon increasing T (open circles in Figure 1b). This discrepancy can arise from a much lower cross-linking degree in our epoxy compared to that reported in the earlier studies.

Forming the epoxy/MLG@TiO_2 composite does not affect the n values remarkably (closed circles and squares in Figure 1b). Meanwhile, increasing the TiO_2 content exhibits the saturation of κ, which shows up prominently above $T \approx 150$ K (squares).

These tendencies may be compared with theoretical and experimental results from the literature. In particular, single-layer graphene nanoribbons follow the $\kappa(T) \propto T^n$ behavior below 100 K with the n value varying from 1.5 to 2.0 for different phonon modes [83,84]. Graphite behaves as $\kappa(T) \propto T^{2.5}$ [85]. The theoretical calculations for the anatase TiO_2 single crystals show that $\kappa(T) \propto T^{-1}$ is within the temperature range of 100–500 K [86] with the dominating Umklapp phonon scattering. For the nanosized anatase particles, about 100 nm

in diameter, the measured temperature dependence of κ exhibits a sinusoidal-like growth below 120 K, followed by a plateau in the range of 120–180 K with $\kappa \approx 0.8$ W m^{-1} K^{-1}, and then it shows a gradual decrease [87].

It can therefore be assumed from the above analysis that the behavior of κ in anatase TiO_2 may have an impact on the saturation observed in the curve with the squares in Figure 1. As the $\kappa_C(T)$ dependence of our epoxy/MLG@TiO_2 composite samples in the whole studied temperature range cannot be explained quantitatively by the temperature behavior of its constituents, the contributions of the filler–polymer interphase regions should then be taken into account. A substantial difference between the open and closed circle data in Figure 1 above $\approx$ 150 K can now be thought to be assigned to the increasing volume of the interphase region with the increasing mass concentrations of the MLG and TiO_2 fillers.

More specifically, to calculate the temperature dependences of $\kappa_{f,eff}(T)$ (see Section 2.2) and to extract the partial contributions of MLG and TiO_2 into Equation (2), the temperature dependence of the Kapitza resistance $R_K(T)$ for all interfaces in the composite is therefore needed to provide basic information for the understanding of the measured $\kappa_C(T)$.

There are two widely used models for evaluating R_K, the acoustic mismatch model (AMM) [88,89] and the diffuse mismatch model (DMM) [85,88,89]. Both models give $R_K(T) \propto T^3$ below 50 K if the phonon dispersion can be neglected [88]. However, the temperature dependence of the acoustic wave velocities incorporated into the models cannot be neglected at an increasing T, even if the velocity dispersion is neglected. Moreover, in the case of graphene, the phonon dispersion of the TA modes, which provide a dominant contribution to R_K, cannot be neglected either. Therefore, it may be expected that the $R_K(T)$ dependence may diverge from the T^3 trend in the temperature range of interest. It has been observed that $R_K(T)$ at the solid–solid interface decreases with an increasing T from 100 to 300 K, with a smaller decreasing rate above 200 K [90]. A decreasing R_K value increases the thermal conductivity of the interphase region.

We may thus assume that a similar temperature behavior of R_K is observed at the graphene–anatase ($R_K \equiv r_{2,1}$), graphene–epoxy ($R_K \equiv r_1$), and anatase–epoxy ($R_K \equiv r_2$) interfaces. Therefore, the increasing κ_C with the increasing T, followed by their saturations at higher loadings, is due not only to the increasing $\kappa_{1,2}$ value but also to the decreasing (stabilizing) $r_{1,2}$. It may be suggested that this methodology can be used to describe $r_1(T)$ at the graphene–epoxy interface and then to incorporate $r_1(T)$, $r_2(T)$, and $r_{2,1}(T)$ in our model. However, a thorough theoretical analysis of $\kappa_C(T)$ is beyond the scope of this study.

2.4. Theoretical Simulation and Numerical Calculations

A great number of theoretical models for evaluating the thermal conductivity of composite materials have been developed [12]. To construct an appropriate model aimed to quantitatively analyze the temperature-loading dependences of κ in our nanocomposites, three assumptions were taken into account:

(1) The polymer matrix contains three solid phases, i.e., MLGs (phase 1), anatase TiO_2 nanoparticles (phase 2), and self-assembled hybrid MLG@TiO_2 nanoparticles (phase 3);

(2) Every particle embedded into the matrix is surrounded by an interphase layer, which has a molecular structure that is determined by the particle–matrix interaction and differs from the polymer structure beyond the layer;

(3) All phases are dispersed randomly and uniformly within the matrix.

We start from the model developed by Su et al. [12], where the authors obtained an algebraic equation to calculate the loading dependence of the thermal conductivity for graphene-filled polymer nanocomposites, taking the thermal boundary resistance into account. To adapt the original model of Su et al. to describe a nanocomposite filled with two-layer ("hybrid") nanoparticles, a certain geometrical configuration of the hybrid particles should be assumed. For the case of graphene-based hybrid nanosheets, a large number of possible configurations have been proposed in the literature (for a brief survey, see, for example, [42]). Here, we use the so-called sandwich-like configuration (SLG) for the

MLG@TiO_2 hybrid nanosheets proposed earlier in ref. [91]. Different geometrical versions of the SLG, including parallelepiped-shaped or spheroid-shaped graphene nanoplatelets assembled with either hard or soft spherical anatase nanoparticles, are given in Figure 3 (see also Supplementary Note S1).

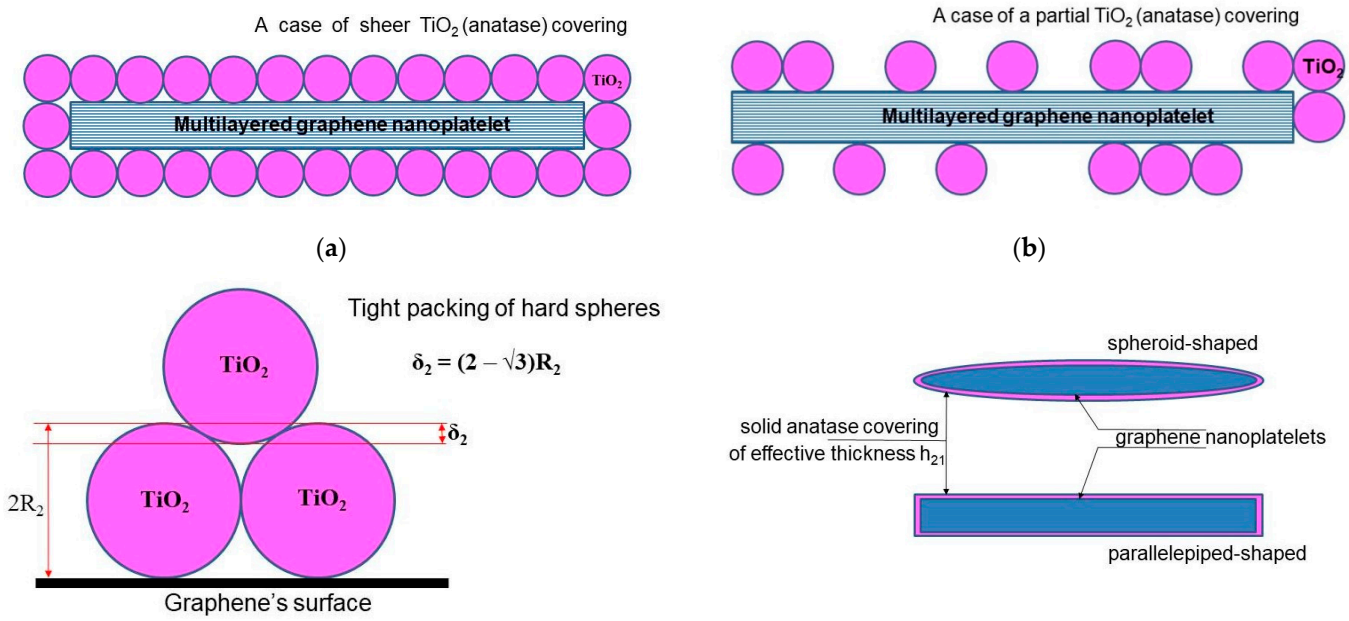


Figure 3. Regular geometrical architectures of hybrid MLG@TiO_2 nanosheets configured in a sandwich-like structure: (**a**) parallelepiped-shaped graphene nanoplatelet covered entirely with hard spherical anatase nanoparticles; (**b**) parallelepiped-shaped graphene nanoplatelet covered partially with hard spherical anatase nanoparticles; (**c**) geometrical effect of tight packing of hard spheres on a flat surface; (**d**) soft-sphere approach to model anatase wrapping of graphene nanoplatelet as a solid layer with the effective thickness of h_{21}.

In our case of a three-phase composite material, the basic equation of the model (see Equation (4) in ref. [12]) takes the following form:

$$\sum_{n=0}^{3} \varphi_n(\rho_n, p_1, p_2, C_1, C_2) \cdot \Phi_n(\{L_n\}, C_1, C_2, r_n, \kappa_n, \kappa_c) = 0 \quad (7)$$

where φ_n represents the volume concentrations of the constituent phases (the subscripts $n = 0$, 1, 2, and 3 correspond to the polymer matrix, free MLG nanoplatelets, free anatase nanoparticles, and hybrid MLG@anatase nanoparticles, respectively) and

$$\sum_{n=0}^{3} \varphi_n = 1.$$

C_1 and C_2 are the mass concentration of graphene nanoplatelets and anatase nanoparticles, respectively, p_1 and p_2 are the relative mass portions of the free (unassembled) MLG and anatase particles, respectively, ($0 \leq p_{1,2} \leq 1$), ρ_n denotes the mass densities, $\{L_{1,2}\}$ is the set of geometrical sizes, $r_{1,2}$ and r_{21} are the Kapitza thermal boundary resistances, κ_n denotes the thermal conductivities (κ_1 includes both in-plane (κ_{g11}) and out-of-plane (κ_{g33}) components), and κ_c is the thermal conductivity of the composite.

The parameters p_1 and p_2 have been introduced to describe the self-assembling effect itself. A case of $p_1 = p_2 = 1$ means that the effect is absent (i.e., the case of two filling phases "1" and "2" in a host matrix), whereas the opposite extreme case of $p_1 = p_2 = 0$

implies complete self-assembling when there is a single (hybrid) constituent phase "1@2" in a matrix. The intermediate situation of $0 < p_{1,2} < 1$ corresponds to a three-phase composite comprising fillers "1" and "2" and their hybrid "1@2". It should be noted, however, that there is no direct evidence for the self-assembling of graphene nanoplatelets and anatase nanoparticles. This will require further experimental evidence to secure the validity of utilizing the self-assembling properties partly because of the fact that the non-oxidized graphene can only exist in a suspension.

The explicit expressions for the functions Φ_n and φ_n are given in Supplementary Notes S1 and S2, respectively. The functions have no obvious physical meaning and are used only to reduce Equation (7) to the compact form. In general, the model incorporates a whole number of both geometrical and material parameters related to the matrix and each constituent phase. The parameters are taken as independent variables to calculate the thermal conductivity κ_C of the composite.

By using the model in the "soft-spheres" approximation, first of all, we complete a fitting procedure to match the calculated values of κ_C to the measured values $\kappa_{C,E}$, supposing that an extreme case of complete self-assembling (i.e., $p_1 = p_2 = 0$) takes place. In doing so, we input κ_m, κ_2, κ_{g33}, and r_1 from Table 1, and then assign fixed values for the interface layers' thicknesses $h_1 = h_2 = 24$ nm, the nanoplatelet's aspect ratio $\alpha = 0.01$ κ_{g11}, r_1 and r_2, and then try to satisfy the target condition in the form $\kappa_C = \kappa_{C,E}$ by varying the graphene–anatase thermal boundary resistance r_{21}. The parameters used in the fitting procedure are summarized in Table 3.

Table 3. Numerical evaluation of graphene@anatase thermal boundary resistance r_{21}.

κ_C (W m^{-1} K^{-1})	κ_{g11} (W m^{-1} K^{-1})	$r_1 \cdot 10^9$ (m^2·K^{-1}·W^{-1})	$r_2 \cdot 10^9$ (m^2·K^{-1}·W^{-1})	$r_{21} \cdot 10^7$ (m^2·K^{-1}·W^{-1})
the case of $\kappa_C(C_1 = 0.01, C_2 = 0.01) = \kappa_{C,E1}$ = (0.2864 ± 5%) W m^{-1} K^{-1}				
$0.95\kappa_{C,E1}$	600.0	3.5	1.0 * (10.0) **	0.923 * (0.699) **
$\kappa_{C,E1}$	600.0	3.5	1.0 (10.0)	0.653 (0.429)
$1.05\kappa_{C,E1}$	600.0	3.5	1.0 (10.0)	0.468 (0.247)
$0.95\kappa_{C,E1}$	1200.0	3.5	1.0 (10.0)	0.971 (0.749)
$\kappa_{C,E1}$	1200.0	3.5	1.0 (10.0)	0.703 (0.481)
$1.05\kappa_{C,E1}$	1200.0	3.5	1.0 (10.0)	0.519 (0.297)
the case of $\kappa_C(C_1 = 0.01, C_2 = 0.05) = \kappa_{C,E2}$ = (0.31295 ± 5%) W m^{-1} K^{-1}				
$0.95\kappa_{C,E2}$	600.0	3.5	1.0 (10.0)	5.447 (4.927)
$\kappa_{C,E2}$	600.0	3.5	1.0 (10.0)	4.476 (3.976)
$1.05\kappa_{C,E2}$	600.0	3.5	1.0 (10.0)	3.745 (3.265)
$0.95\kappa_{C,E2}$	1200.0	3.5	1.0 (10.0)	5.618 (5.131)
$\kappa_{C,E2}$	1200.0	3.5	1.0 (10.0)	4.644 (4.185)
$1.05\kappa_{C,E2}$	1200.0	3.5	1.0 (10.0)	3.917 (3.472)

* The values of r_{21} without the brackets correspond to r_2 without the brackets. ** The values in brackets represent appropriate r_2 and r_{21} values.

As expected from Table 3, the resulting values of r_{21} do not depend on r_1. Since the numerical values for r_2 are lacking in the literature, they were varied by up to one order of magnitude (the values in the brackets and without the brackets in Table 3). Decreasing r_2 increases r_{21} from 11% to 12.6% for C_1:C_2 = 0.01:0.01 or from 46% to 52% for C_1:C_2 = 0.01:0.05, where the smaller percentages correspond to lower κ_{g11} values. One can also see that the certain increment in r_{21} is achieved while κ_{g11} is doubled from 600 to 1200 W·m^{-1}·K^{-1}. The resulting magnitude of r_{21} (from about 0.25×10^{-7} to 0.62×10^{-7} m^2·K^{-1}·W^{-1}) seems to be

appropriate. We can, for example, compare this value with the calculated room-temperature thermal boundary resistance of the Cu/Si interface, which is 5×10^{-4} $m^2 \cdot K^{-1} \cdot W^{-1}$ [90].

Experimentally, it is rather difficult to distinguish between the thermal resistance of a thin layer and the thermal resistance of the substrate. Zheng et al. [92] treated the graphite/Ni interfaces as one effective layer and fit the time domain thermoreflectance (TDTR) data to two free parameters. A total interface thermal resistance of $\approx 2.3 \times 10^{-8}$ $m^2 \cdot K^{-1} \cdot W^{-1}$ was obtained. The effective cross-plane thermal conductivity of ≈ 3.3 W m^{-1} K^{-1} was reported, whereas the in-plane thermal conductivity varied between ≈ 650 and 1000 W m^{-1} K^{-1}.

Multilayered graphene nanoplatelets typically contain structural defects, including point and edge defects, surface wrinkles, mesovoids, etc. The effects of defects on the interface's thermal conductivity in graphene/epoxy composites were observed by employing molecular dynamics simulations [93]. Among the various defect types, Stone–Wales defects are the most effective in improving the interface's thermal conductivity in the composite. This is due to the enhanced vibration intensity of the out-of-plane low-frequency phonons, which could enhance the phonon coupling between the epoxy and graphene, thus increasing the conductivity. In turn, increasing the number of graphene layers in the MLG enhances the phonon scattering, thus decreasing the thermal conductivity. When the layer number exceeds four, the MLG properties become close to that of graphite, and the interface thermal conductivity stabilizes at the value close to that of graphite.

The variation in the interfacial thermal resistance with respect to the functionalization, isotope, and acetylenic linkages in graphene is also systematically examined using molecular dynamics [94]. The graphene–epoxy interfacial thermal resistance can be remarkably reduced by using the covalent and noncovalent functionalization. Among different functional groups, covalent butyl is the most effective substance in reducing the resistance.

Strictly speaking, the thermal boundary resistance for the in-plane graphene–epoxy interface ($r_{1X} = r_{1Y}$) differs from the cross-plane resistance (r_{1Z}) (see Supplementary Note S1). These should be completely different thermal contacts since the graphene phonon density of states is shifted to a higher energy due to the in-plane vibration compared to the cross-plane case. The sound velocity is also significantly different in the in-plane and cross-plane configurations. Meanwhile, an average value r_{1av} of r_1 can only be measured because the partial contributions of r_{1X} and r_{1Z} cannot be separated from each other. To obtain a quantitative estimate of the error incurred on the approximation of $r_1 \approx r_{1X} = r_{1Z}$, the value of r_{1av} for parallelepiped-shaped graphene nanoplatelets can be expressed as

$$\frac{1}{r_{1av}} = \frac{\frac{L_X L_Z}{r_{1X}} + \frac{L_Y L_Z}{r_{1Y}} + \frac{L_X L_Y}{r_{1Z}}}{L_X L_Z + L_Y L_Z + L_X L_Y}. \quad (8)$$

Inputting $r_{1X} = r_{1Y}$, $L_Z = 50$ nm, $L_X = L_Y = 5 \times 10^3$ nm (average linear dimensions of our nanoplatelets) yields $r_1 \approx 1.0144 \cdot r_{1Z}$ (see Supplementary Note S1). Thus, approximating $r_1 \approx r_{1X} = r_{1Z}$ would result in a negligible error in the calculation of the thermal conductivity κ_C of the graphene–epoxy nanocomposites. One may expect that the error might be even less in the hybrid graphene@anatase TiO_2 composite due to the thermal screening of graphene nanoplatelets by titanium dioxide fillers. Therefore, exploiting the case $r_{1X} \neq r_{1Y}$ may seem, at first glance, to not bring any new qualitative conclusions compared to those given above.

We note that the properties of composites appear to depend not only on the size but also on the aspect ratio of the fillers α. It turns out that the interphase layer thicknesses, h_1 and h_2, are sensitive to the polymer molecular structure and surface reactivity of the fillers.

One can therefore consider the dependence of r_{21} on the aspect ratio α of the MLGs at varying $h_1 = h_2$, as shown in Figure 4. It is seen that the value of r_{21} depends rather sensitively on the magnitude of α, especially at a high $\alpha > 200$, when the nanoplatelets can be considered as nanoribbons. In contrast, r_{21} depends only slightly on h_1 and h_2 in the range of 10.0 nm $\leq h_1, h_2 \leq$ 30.0 nm.

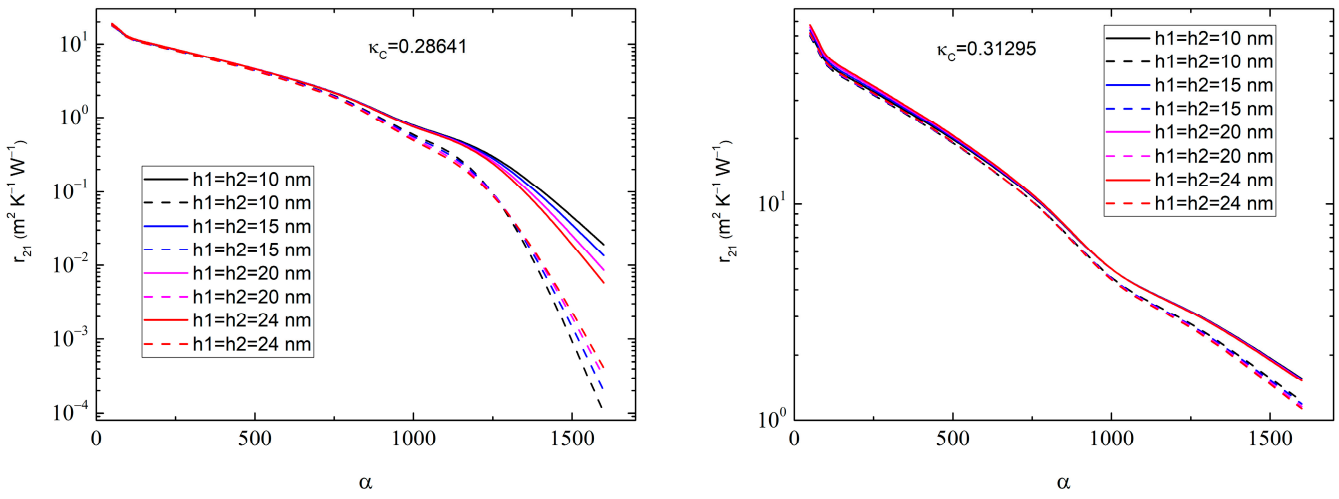


Figure 4. Graphene–anatase thermal boundary resistance r_{21} as a function of graphene aspect ratio α for (**a**) C_1:C_2 = 0.01:0.01, $\kappa_C = \kappa_{C,E1} = 0.2864$ W·m^{-1}·K^{-1} and (**b**) C_1:C_2 = 0.01:0.05, $\kappa_C = \kappa_{C,E2} = 0.31295$ W·m^{-1}·K^{-1}. Different colors correspond to various values of interphase layer thicknesses: $h_1 = h_2 = 10$ nm (black curves), 15 nm (blue curves), 20 nm (magenta curves), and 24 nm (red curves). Solid lines correspond to $r_2 = 1.0 \times 10^{-9}$ m^2·K^{-1}·W^{-1} and dashed lines correspond to $r_2 = 1.0 \times 10^{-8}$ m^2·K^{-1}·W^{-1}. The MLG thickness is $L_Z = 50.0$ nm, whereas $L_X = L_Y = \alpha L_Z$.

The results in Figure 4 may help to increase the accuracy in the experimental determination of r_{21}. To carry this out properly, one first needs to obtain the distribution function $F(\alpha)$ of the MLGs. Averaging the basic Equation (7) over an interval of $F(\alpha)$ will then give the value of r_{21}, which, however, is beyond the scope of this paper.

It should be borne in mind that, to make numerical estimates of the impacts of the interphase layers on the structural characteristics of a three-phase polymer nanocomposite using the relations given in Supplementary Note S1, it is necessary, in addition to the empirical parameters p_1 and p_2, to predict two independent quantitative parameters of the interphase layers, namely the volume fractions $\varphi_{i1,2}$ and mass densities $\rho_{i1,2}$. Conducting an experimental evaluation of $p_{1,2}$ is a difficult task. They depend on the technique used to prepare the graphene–anatase solution and the adhesion properties of the interacting surfaces. The actual process of self-assembling is stochastic, and different nanoplatelets have different covering degrees and spotted structures. It is evident that the probability of formation of each subsequent anatase layer decreases. Therefore, we may expect an increasing $p_{1,2}$ value when the occupation of platelets increases with the enhancing C_2 and input either a linear or exponential approximation for the $p_{1,2}(C_2)$ dependence.

We therefore suppose that the assumption of the constant values of $p_{1,2}$ at low loadings will give us essential physical insight. There is, of course, an uncertainty in choosing p_1 and p_2. However, we may avoid the ambiguity in the numerical estimates by inputting $p_1 = p_2$ when the geometrical characteristics of the hybrid nanoparticle become independent of both p_1 and p_2.

For simplicity, we postulate that the layer's shape is similar to that of the nanoparticle itself, and the layer's spatial structure is homogeneous along the surface of the nanoparticle and varies only along the surface's normal direction. With such an assumption, $\varphi_{i1,2}$ can be determined in terms of the particle dimensions and layer thicknesses $h_{i1,2}$ (see Supplementary Note S1). The molecular dynamic simulations testify that the h_i values are limited to about $2R_G$, with R_G being the radius of gyration of the polymer matrix [95,96]. This restriction on h_i is a logical consequence of the assumption that the formation of the interphase layer occurs only as a result of the effects of the molecular adhesive forces on the polymer–nanoparticle interface. For instance, for the DGEBA epoxy resins cured with tri-

ethylenetetramine (TETA) hardener ($C_6H_{18}N_4$), the R_G value estimate is 10–14 nm [97]. The radius R_G depends on cyclic deformation characteristics such as the operation frequency and loading direction used in the molecular dynamics simulations. Therefore, without the loss of generality, we assume that $h_1 = h_2$ and input $h_1 = h_2 = 24$ nm, supposing an average value of 12 nm for R_G. The numerical calculations show that an increasing h_i value will result in an increase in the nanocomposite's thermal conductivity κ_C.

As for the values of $\rho_{i1,2}$, they obviously cannot diverse considerably from the epoxy density ρ_0. The earlier molecular dynamic simulations showed that a range of polymer density fluctuations depends on the nature of the molecular interactions between a filling particle and the polymer macromolecules and it is mainly localized in the close vicinity of the particle of about a few angstroms [98]. On the other hand, using simple considerations based on the free volume concept of the polymer structure allowed us to evaluate the upper limit for the interface layer density for the DGEBA epoxies as $1.064\rho_0$ [4]. Therefore, we assume $0.95\rho_0 \leq \rho_{i1,2} \leq 1.05\rho_0$ to evaluate $\varphi_{i1,2}$. This spread in the value of ρ appears to cause a negligible impact on the calculation results.

For example, if it is assumed that $p_1 = 0.05$ and $p_2 = 0.05$, one obtains only a 0.0145% variation in the density ρ_C of the composite for the case of $(C_1, C_2) = (0.01, 0.01)$ and 0.035% for $(C_1, C_2) = (0.01, 0.05)$. For the case of $h_1 = h_2 = 10$ nm and $p_1 = p_2$, the calculated values of the interphase layer factors are $F_1 = 0.4112$, $F_2 = 1.744$, $F_3(0.01, 0.01) = 0.1163$, and $F_3(0.01, 0.05) = 0.2654$.

Table 4 gives the values of the filler's ($\varphi_{1,2,3}$) and layer's ($\varphi_{i1,2}$) volume concentrations, which were calculated by using Equations (S38)–(S44) in Supplementary Note S2. The difference $\Delta\varphi_n(p_1, p_2) = \varphi_n(p_1, p_2, \rho_{i1} = 1.05\rho_0, \rho_{i2} = 1.05\rho_0) - \varphi_n(p_1, p_2, \rho_{i1} = 0.95\rho_0, \rho_{i2} = 0.95\rho_0)$ increases with the increasing $p_1 = p_2$ and reaches its maximal value of $1.67{\cdot}10^{-5}$ for the case of $p_1 = p_2 = 1.0$, $n = 1$, $C_1 = 0.01$, $C_2 = 0.05$. One can see that the interphase areas occupy even greater volume in the composite compared to that in the fillers,

$$\varphi_{i1} + \varphi_{i2} > \varphi_1 + \varphi_2 + \varphi_3,$$

only if $p_1 = p_2 = 1.0$ when $\varphi_3 = 0$, although the above interphase layer thicknesses of $h_1 = h_2 = 10$ nm are not so large.

Table 4. Volume concentrations of the filler ($\varphi_{1,2,3}$) and interphase layer ($\varphi_{i1,2}$). Top and bottom values correspond to $\rho_{i1} = \rho_{i2} = 0.95\rho_0$ and $\rho_{i1} = \rho_{i2} = 1.05\rho_0$, respectively.

p_1	p_2	φ_1	φ_2	φ_3	$\varphi_1 + \varphi_2 + \varphi_3$	φ_{i1}	φ_{i2}	$\varphi_{i1} + \varphi_{i2}$
$C_1 = 0.01, C_2 = 0.01$								
0	0	0 0	0 0	8.4889×10^{-3} 8.4898×10^{-2}	8.4889×10^{-3} 8.4898×10^{-2}	0 0	1.1266×10^{-3} 1.1268×10^{-3}	1.1266×10^{-3} 1.1268×10^{-3}
0.05	0.05	2.6799×10^{-4} 2.6803×10^{-4}	1.5644×10^{-4} 1.5647×10^{-4}	8.0643×10^{-3} 8.0655×10^{-2}	8.4877×10^{-3} 8.1092×10^{-2}	1.1020×10^{-4} 1.1022×10^{-4}	1.3431×10^{-3} 1.3433×10^{-3}	1.4533×10^{-3} 1.4537×10^{-3}
0.50	0.50	2.6795×10^{-3} 2.6807×10^{-3}	1.5642×10^{-3} 1.5690×10^{-3}	4.2437×10^{-3} 4.2456×10^{-2}	8.4874×10^{-3} 4.6706×10^{-2}	1.1019×10^{-3} 1.1024×10^{-3}	3.2912×10^{-3} 3.2927×10^{-3}	4.3931×10^{-3} 4.3951×10^{-3}
1.00	1.00	5.3581×10^{-3} 5.3602×10^{-3}	3.1279×10^{-3} 3.1303×10^{-3}	0 0	8.4860×10^{-3} 8.4905×10^{-3}	2.2034×10^{-3} 2.2051×10^{-3}	5.4250×10^{-2} 5.4592×10^{-2}	5.6453×10^{-2} 5.6797×10^{-2}
$C_1 = 0.01, C_2 = 0.05$								
0	0	0 0	0 0	2.1608×10^{-2} 2.1612×10^{-2}	2.1608×10^{-2} 2.1612×10^{-2}	0 0	2.0947×10^{-3} 2.0952×10^{-3}	2.0947×10^{-3} 2.0952×10^{-3}
0.05	0.05	2.7567×10^{-4} 2.7577×10^{-4}	8.0463×10^{-4} 8.0543×10^{-4}	2.0526×10^{-2} 2.0533×10^{-2}	2.1606×10^{-2} 2.1614×10^{-2}	1.1336×10^{-4} 1.1338×10^{-4}	3.3931×10^{-3} 3.3943×10^{-3}	3.5065×10^{-3} 3.5077×10^{-3}
0.50	0.50	2.7550×10^{-3} 2.7594×10^{-3}	8.0412×10^{-3} 8.0543×10^{-3}	1.0796×10^{-2} 1.0814×10^{-2}	2.1592×10^{-2} 2.1628×10^{-2}	1.1329×10^{-3} 1.1347×10^{-3}	1.5071×10^{-2} 1.5095×10^{-2}	1.6204×10^{-2} 1.6230×10^{-2}
1.00	1.00	5.5060×10^{-3} 5.5227×10^{-3}	1.6071×10^{-2} 1.6120×10^{-2}	0 0	2.1577×10^{-2} 2.1643×10^{-2}	2.2642×10^{-3} 2.2711×10^{-3}	2.8028×10^{-2} 2.8113×10^{-2}	3.0292×10^{-2} 3.0384×10^{-2}

It can be concluded from these calculations that the chosen sizes of the filler's loading allow one to avoid the interphase layer overlap and percolation effects. This will be discussed further below.

The overlapping effect can be avoided at low values of $C_{1,2}$. Indeed, the average distance L_P between adjacent nanoparticles (with linear dimension R_P whose volume fraction φ_p is distributed homogeneously within the polymer matrix) can be approximated by [99]

$$L_p(C_1, C_2) = R_p\left\{\left[\frac{4\pi}{3\varphi_p(C_1, C_2)}\right]^{1/3} - 2\right\}, \quad (9)$$

where the values of $\varphi_p(C_1, C_2)$ can be evaluated by using the relations given in Supplementary Note S2. By taking $R_P = 25$ nm for the anatase nanoparticles and inputting $\varphi_p = \varphi_1(p_1 = p_2 = 1.0, C_1 = 0.01, C_2 = 0.05) = 5.513 \times 10^{-3}$, we find a minimal value of $L_2 \approx 55$ nm. An extreme case of $L_{2,min} = 2h_2 = 20.0$ nm occurs at $C_{2,max} = 0.2407$. For graphene nanoplatelets with $R_P = \frac{L_2}{2} = 25$ nm, we obtain a similar result, $L_{1,min} = 2h_1 = 20.0$ nm at $C_{1,max} = 0.2556$.

The percolation thresholds for graphene nanoplatelets occur at the values of $C_{1,PT0}(C_2)$, which are much lower than those of $C_{1,max}$. Supposing that epoxy is an ideal insulator, the percolation threshold φ_{PT} of a composite filled with randomly oriented oblate-shaped ellipsoidal particles is [100]

$$\varphi_{PT}(\alpha) = \frac{9S_{33}(\alpha)[1 - S_{33}(\alpha)]}{-9S_{33}^2(\alpha) + 15S_{33}(\alpha) + 2}, \quad (10)$$

where S_{33} can be found from Equation (S11) in Supplementary Note S1. For our uncovered graphene nanoplatelets, $\alpha = 0.01$ and $\varphi_{PT} = \varphi_{PT0} = 0.01708$, which corresponds to the mass concentrations of $C_{1,PT0}$ =0.031545 if $C_2 = 0.01$ or $C_{1,PT0} = 0.030667$ if $C_2 = 0.05$, provided that $p_1 = p_2 = 1.0$ (i.e., when no assembling occurs) and $\rho_{i1} = \rho_{i2} = \rho_m$. To calculate $C_{1,PT0}$, one should use Equation (S39) in Supplementary Note S2 and insert φ_{PT0} instead of φ_1 and $\rho_C(C_1, C_2)$ from Equation (S37) in Supplementary Note S2.

Combining the single anatase covering layer with the "hard-spheres" approach yields $\alpha(R_2) = (L_Z + 2R_2)/(L_X + 2R_2) = 150/5100 = 0.02941$ and $\varphi_{3PT}(\alpha(2R_2)) = \varphi_{3PT,max} = 0.04718$ as extreme values of the percolation threshold for the hybrid MLG@TiO_2 nanosheets.

In contrast, when the "soft-spheres" model is employed, the anatase covering thickness $h = h(C_1, C_2)$ is a continuous function of both C_1 and C_2, whereas $\alpha = \alpha(h) = (L_Z + 2h)/(L_X + 2h)$ is a continuous function of h. Then, φ_{3PT} can be derived from

$$\varphi_1(p_1, p_2, C_1, C_2) = \varphi_{3PT}(\alpha(h)),$$

where h is a solution of

$$N_{21}(p_1, p_2, C_1, C_2)\cdot v_2 = \frac{1 - p_2}{1 - p_1}\cdot\frac{C_2}{C_1}\cdot\frac{\rho_1}{\rho_2}\cdot v_1 = \frac{\pi}{6}(L_X + 2h)^2(L_z + 2h) - v_1, \quad (11)$$

with $v_1 = v_{1,1}$ and $v_1 = v_{1,2}$ given by Equations (S23) and (S24) in Supplementary Note S1 for parallelepiped- and spheroid-shaped nanoplatelets, respectively. The numerical solution of Equation (11) for $p_1 = p_2 = 0$ (complete assembling) gives the set of values of the percolation thresholds presented in Table 5 for the concentrations that are reachable in our experimental samples.

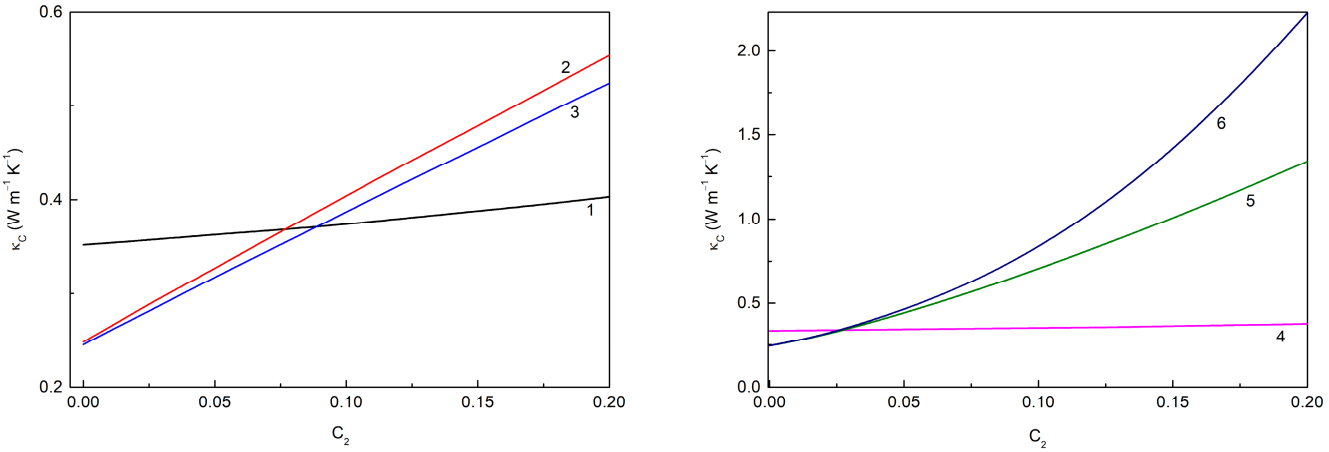
Interestingly, varying the mass density $\rho_{i1,2}$ by 5% around the value of ρ_m at $C_1 = 0.01$ and $C_2 = 0.05$ caused the percolation threshold to change to not more than 0.01% and 0.023% for the parallelepiped- and spheroid-shaped configurations, respectively. It is apparent, therefore, that the effects of the interphase layer overlaps, and percolation cannot be deduced from the experimental κ data.

Table 5. Percolation thresholds ($\varphi_{3,PT}$) for hybrid MLG@TiO_2 nanosheets in MLG@TiO_2-epoxy nanocomposites in cases of parallelepiped (p)- and spheroid (s)-shaped configurations.

Configuration	C_2	h (nm)	$\alpha(h)$	$C_{1,PT}$	$\varphi_{3,PT}$
p-shaped	0.01	4.585	0.0118	0.03121	0.02006
p-shaped	0.05	24.54	0.0196	0.02916	0.03248
s-shaped	0.01	4.571	0.0118	0.03119	0.02005
s-shaped	0.05	24,30	0.0195	0.02890	0.03233

2.5. Discussing the Loading Dependencies

Figure 5 shows the loading dependencies of the thermal conductivities of the MLG@TiO_2-epoxy nanocomposites calculated for different cases of interphase interactions. Figure 5a corresponds to the case when the filler–epoxy macromolecule interactions are neglected so that interphase layers cannot be formed. If the fillers remain unassembled, curve 1 is reproduced. In the opposite case of the fillers that are fully assembled in hybrid particles, curves 2 and 3 are obtained. A summary of the data in Figure 5a shows the following trends:



(**a**) (**b**)

Figure 5. Loading dependencies of the thermal conductivity κ_C of MLG@TiO_2-epoxy nanocomposites calculated for different cases of interphase interactions (**a**) without interphase layers (($h_1 = 0, h_2 = 0$), $\kappa_{g11} = 600.0$ W m^{-1} K^{-1}, $\kappa_{g33} = 6.0$ W m^{-1} K^{-1}: curve 1—non-assembled particles ($p_1 = p_2 = 1.0$) (κ_C is independent of r_{21}); curve 2—fully assembled particles ($p_1 = p_2 = 0$), $r_{21} = 1.3536 \times 10^{-7}$ m^2 K W^{-1}; curve 3—fully assembled particles ($p_1 = p_2 = 0$), $r_{21} = 1.5310 \times 10^{-7}$ m^2 K W^{-1}) and (**b**) with interphase layers (($h_1 = h_2 = 10$ nm), $\kappa_{g11} = 600.0$ W m^{-1} K^{-1}, $\kappa_{g33} = 6.0$ W m^{-1} K^{-1}: curve 4—non-assembled particles ($p_1 = p_2 = 1.0$); curve 5—fully assembled particles ($p_1 = p_2 = 0$), $r_1 = 3.5 \times 10^{-9}$ m^2 K W^{-1}, $r_2 = 1.0 \times 10^{-8}$ m^2 K W^{-1}, $r_{21} = 1.5310 \times 10^{-7}$ m^2 K W^{-1}; curve 6—fully assembled particles ($p_1 = p_2 = 0$), $r_1 = 3.5 \times 10^{-9}$ m^2 K W^{-1}, $r_2 = 1.0 \times 10^{-9}$ m^2 K W^{-1}, $r_{21} = 1.3536 \times 10^{-7}$ m^2 K W^{-1}).

(1) κ_C increases with the increasing C_2 regardless of whether or not the assembling effect occurs;

(2) The particle assembling decreases κ_C, and the greater the assembling degree $p_1 + p_2$, the smaller the observed κ_C value;

(3) κ_C decreases with the increasing graphene–anatase thermal boundary resistance r_{21}, i.e., with the weakening of the MLG-TiO_2 interphase interaction.

It is also interesting to note that κ_C increases with the increasing κ_{g11}, κ_{g33} or κ_2 values, as expected.

Figure 5b represents the case when the fillers interact with the epoxy macromolecular chains, and thus, interphase layers are formed. Curve 4, similarly to curve 1, corresponds

to unassembled fillers, while curves 5 and 6 correspond to fully assembled fillers. One can see that including an interphase layer results in a decreasing κ_C value. The other trends deduced from Figure 5a are also seen in Figure 5b.

Figure 6 shows the dependencies of κ_C in the composite with fully assembled graphene and anatase particles on the thermal boundary resistance at the graphene–anatase interface (r_{21}) computed at the fixed values of the thermal boundary resistance at the anatase–epoxy interface (r_2). As expected, a decreasing r_{21} value results in a rapid increase in κ_C. Instead, it is useful to note that decreasing the r_2 value (or increasing either C_2 or κ_{g11}) increases the ratio $\kappa_C(r_{21min})/\kappa_C(r_{21max})$, e.g., 1.43 for $r_2 = 1.0 \times 10^{-7}$ m^2 K W^{-1} (curves 3 and 9 in Figure 6) against 6.51 for $r_2 = 1.0 \times 10^{-9}$ m^2 K W^{-1} (curve 10).

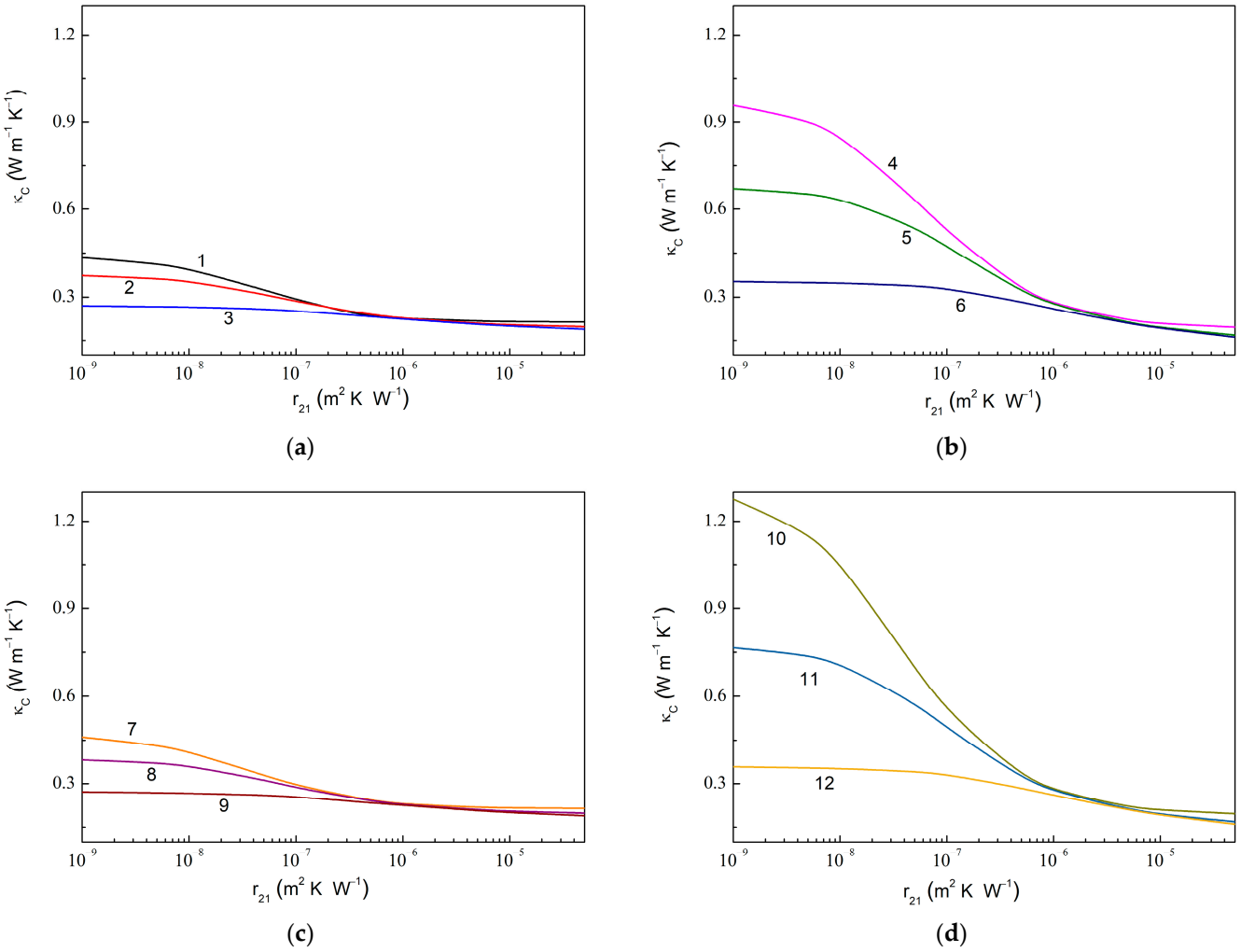


Figure 6. Thermal conductivity of MLG@TiO_2-epoxy nanocomposites vs. thermal boundary resistance r_{21} at graphene–anatase interface calculated at fixed values of the thermal boundary resistance r_2 at anatase–epoxy interface for the case of fully assembled graphene and anatase particles at (**a**) $C_1 = 0.010$, $C_2 = 0.010$, $\kappa_{g11} = 600.0$ W m^{-1} K^{-1}, $\kappa_{g33} = 6.0$ W m^{-1} K^{-1}; (**b**) $C_1 = 0.010$, $C_2 = 0.050$, $\kappa_{g11} = 600.0$ W m^{-1} K^{-1}, $\kappa_{g33} = 6.0$ W m^{-1} K^{-1}; (**c**) $C_1 = 0.010$, $C_2 = 0.010$, $\kappa_{g11} = 1200.0$ W m^{-1} K^{-1}, $\kappa_{g33} = 6.0$ W m^{-1} K^{-1}; and (**d**) $C_1 = 0.010$, $C_2 = 0.050$, $\kappa_{g11} = 1200.0$ W m^{-1} K^{-1}, $\kappa_{g33} = 6.0$ W m^{-1} K^{-1}. The values of r_2 are 1.0×10^{-9} m^2 K W^{-1} (curves 1, 4, 7, and 10), 1.0×10^{-8} m^2 K W^{-1} (curves 2, 5, 8, and 11), and 1.0×10^{-7} m^2 K W^{-1} (curves 3, 6, 9, and 12).

Figure 7 shows similar dependencies upon r_2 at fixed values of r_{21}. The computed results show a similar trend, as observed in Figure 6. Thus, an increased κ_C value is observed upon the decreasing r_2 value, while an increased $\kappa_C(r_{2min})/\kappa_C(r_{2max})$ value is realized with the decreased r_{21}, increased C_2, or increased κ_{g11}, from 1.55 for $r_{21} = 1.0 \times 10^{-7}$ m^2 K W^{-1}

(curves 3 and 9 in Figure 7) to 7.76 for $r_{21} = 1.0 \times 10^{-9}$ m^2 K W^{-1} (curve 10). Remarkably, a sensitivity of κ_C to varying κ_{g11} increases with the increasing C_2.

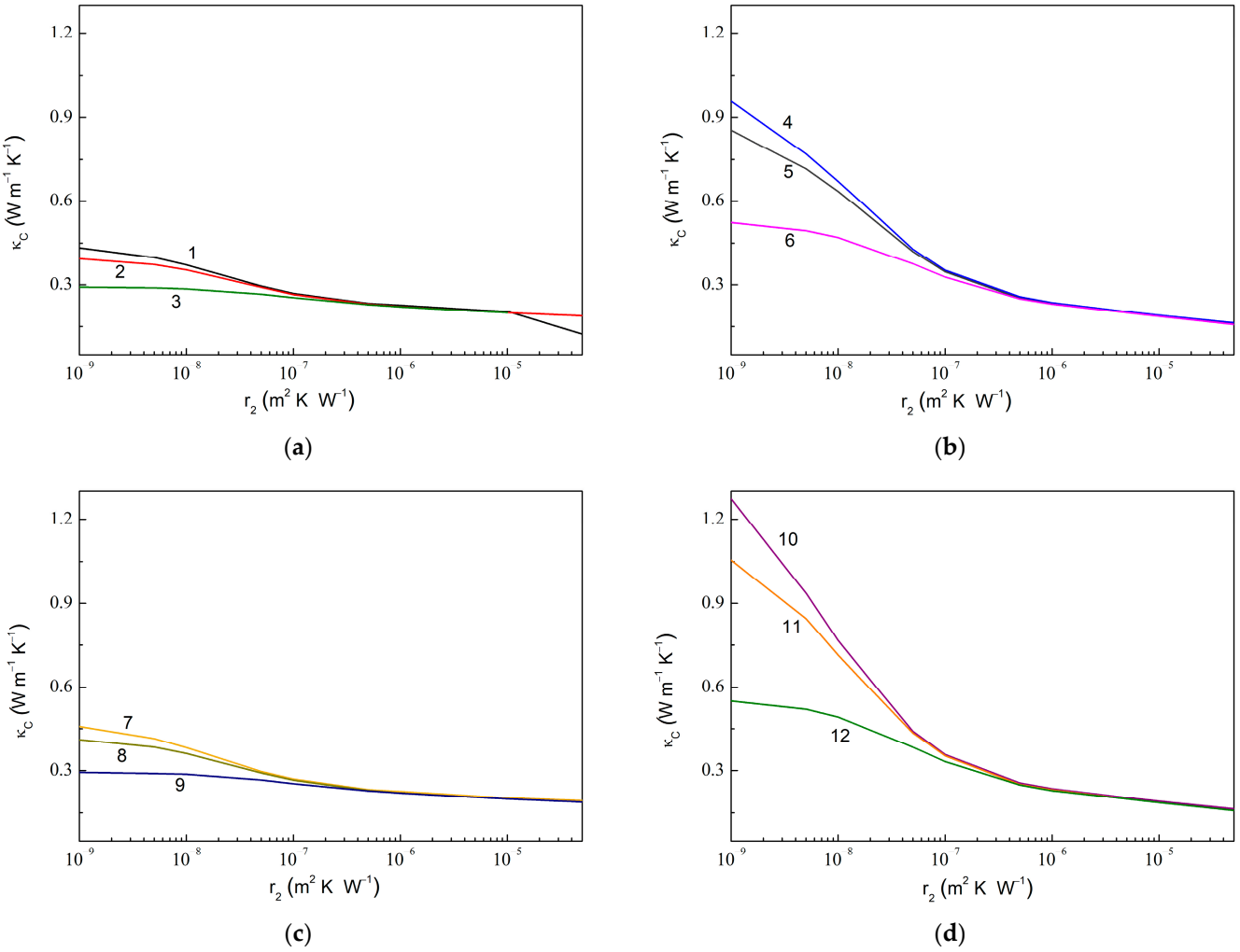


Figure 7. Same dependencies as in Figure 6 but upon varying r_2 and fixed r_{21}. (**a**) $C_1 = 0.010$, $C_2 = 0.010$, $\kappa_{g11} = 600.0$ W m^{-1} K^{-1}, $\kappa_{g33} = 6.0$ W m^{-1} K^{-1}; (**b**) $C_1 = 0.010$, $C_2 = 0.050$, $\kappa_{g11} = 600.0$ W m^{-1} K^{-1}, $\kappa_{g33} = 6.0$ W m^{-1} K^{-1}; (**c**) $C_1 = 0.010$, $C_2 = 0.010$, $\kappa_{g11} = 1200.0$ W m^{-1} K^{-1}, $\kappa_{g33} = 6.0$ W m^{-1} K^{-1}; and (**d**) $C_1 = 0.010$, $C_2 = 0.050$, $\kappa_{g11} = 1200.0$ W m^{-1} K^{-1}, $\kappa_{g33} = 6.0$ W m^{-1} K^{-1}. The values of r_{21} are 1.0×10^{-9} m^2 K W^{-1} (curves 1, 4, 7, and 10), 1.0×10^{-8} m^2 K W^{-1} (curves 2, 5, 8, and 11), and 1.0×10^{-7} m^2 K W^{-1} (curves 3, 6, 9, and 12).

A general expression for the effective thermal conductivity $\kappa_{f,eff}$ of a particle embedded into a polymer matrix has been obtained in [101] in the effective media approximation. We have used this expression to write $\kappa_{f,eff}$ for free anatase particles ($\kappa_{2,eff}$, Equation (S8) in Supplementary Note S1), free graphene platelets ($\kappa_{g11,eff}$ and $\kappa_{g33,eff}$, Equation (S11)), and hybrid graphene@anatase particles ($\kappa_{h,eff}$, Equation (S14)).

Figure 8 shows the dependencies of normalized effective thermal conductivities of filling particles embedded into epoxy on correspondent thermal boundary resistances.

Thus, as expected, the effective thermal conductivities of the filling particles increase with the decreasing r value because this decrease is accompanied by an increased conductivity κ_{int} of the interphase layers given by Equation (6).

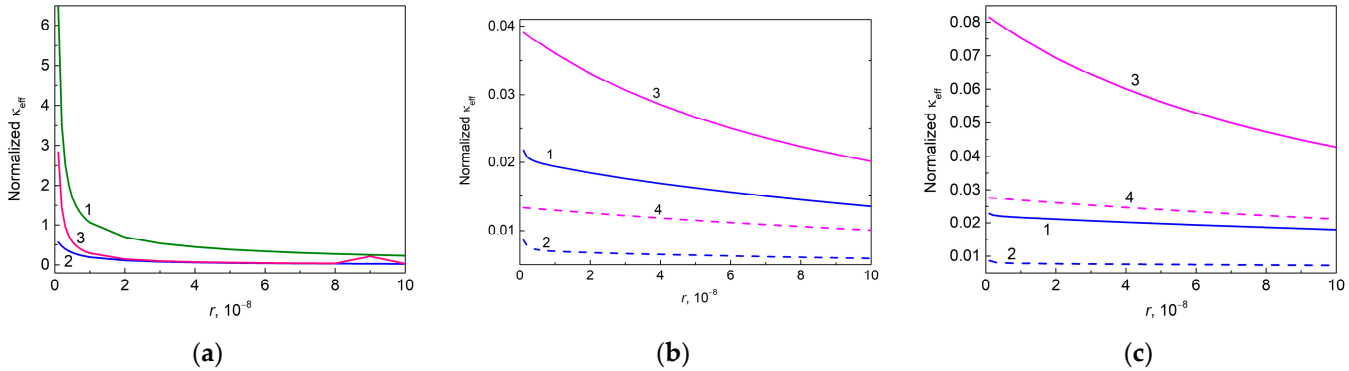


Figure 8. Normalized thermal conductivity of filling particles embedded into epoxy as a function of thermal boundary resistance, calculated by using Equations (S8), (S11), and (S14) in Supplementary Note S1, (**a**) for free particles of anatase (curve 1, $\kappa_{a,eff}/0.455$, $r = r_2$) and graphene (curve 2, $\kappa_{g11,eff}/600.0$, $r = r_1$) (curve 3, $\kappa_{g33,eff}/6.0$, $r = r_1$); (**b**) for hybrid graphene@anatase particles ($p_1 = p_2 = 0$, $C_1 = 0.010$, $C_2 = 0.010$): $\kappa_{h11,eff}/600.0$ (curves 1 and 2) and $\kappa_{h33,eff}/6.0$ (curves 3 and 4); and (**c**) for hybrid graphene@anatase particles ($p_1 = p_2 = 0$, $C_1 = 0.010$, $C_2 = 0.050$): $\kappa_{h11,eff}/600.0$ (curves 1 and 2) and $\kappa_{h33,eff}/6.0$ (curves 3 and 4). Solid and dashed lines in (**b**,**c**) correspond to $r_{21} = 1.0 \times 10^{-7}$ m^2 K W^{-1} and 3.0×10^{-7} m^2 K W^{-1}, respectively.

It should be mentioned that the curves presented in Figures 6 and S2 predict the bounds for κ_C, where they can be tailored by varying the thermal boundary resistances, r_2 and/or r_{21} (in the case of complete self-assembling), if both C_1 and C_2 remain unchanged.

Evidently, the value of the thermal boundary resistance at the filler–polymer interface (r_1 and r_2 in our case) can vary via the chemical modification of the surfaces of the filling particles. This surface functionalization involves the conjugation of suitable functional molecular groups with the active surface sites of the particles. Generally speaking, the functionalization of fillers with the requisite moieties depends on the chemistry of the fillers. Recently, efficient techniques for the functionalization of carbon nanomaterials were developed (see refs. [102,103] and references therein), the most important of which may be classified as either covalent or non-covalent functionalization.

Covalent functionalization alters the state of bond connectivity between the fillers and a host polymer matrix. The functional groups form the covalent linkage between the polymer's macromolecules and the dangling carbon bonds located on the skeletons of graphene nanoplatelets (mainly on its edges and in structural defects). For example, the covalent interactions of oxidized graphene's basal and lateral surfaces with epoxy are dominated by hydroxyl, epoxy, and carboxylic molecular groups [104]. As a result of functionalization, the translational symmetry of the outer graphene nanosheets of MLG-nanoplatelets is disrupted by changing the sp^2 carbon atoms to sp^3 carbon atoms, and both the electronic and phonon transport properties of the sheets are influenced.

Moreover, an enhanced conjugation between fillers and a host polymer matrix can happen through noncovalent interactions by attaching some specific secondary ligands on the filler's surface. Various approaches of filler-to-ligand noncovalent binding include electrostatic interaction, π-π stacking, and H-bonding [103]. For MLG fillers, noncovalent functionalization, in contrast to covalent functionalization, has no effect on the π-π stacking of the multilayered nanoplatelet [105].

The grafted individual moieties or ligand-moiety chains in a functionalized filler can act as heat transfer channels between the filler and a host polymer matrix, decreasing phonon scattering at this interface and thus reducing the thermal boundary resistance r or increasing the heat exchange between the filler and the matrix [106,107]. In other words, grafted species increase the overlapping phonon density of states of the functionalized filler and the polymer matrix.

On the other hand, the surface functionalization breaks the regular surface structure of the fillers and reduces the intrinsic mean free path length of the phonons, acting as additional scattering centers for the phonons. Molecular dynamic simulations showed that the in-plane thermal conductivity of infinitely long graphene nanoribbons (κ_∞) decreases sharply with the increasing the grafting density g_d [107]. Specifically, κ_∞ reduces to about 14% from that for ungrafted graphene at $g_d = 1.6\%$. Furthermore, the thermal conductivity of grafted graphene at $g_d = 12.5\%$ is only 3.86% of that for ungrafted graphene. Qualitatively similar effects may be expected for graphene functionalized by anatase nanoparticles.

Therefore, the impact of the filler functionalization on the composite's thermal conductivity appears to be twofold due to the competition between these two phenomena, an enhanced thermal conductance at the interface and the reduced intrinsic thermal conductivity of the filler. A certain optimal value $g_{d,\mathrm{opt}}$ may be expected for filling particles, which is required to maximize the ratio $\kappa_C\left(g_{d,\mathrm{opt}}\right)/\kappa_C(g_d = 0)$.

We can further extend the relevance of this model by providing the way in which these functionalization mechanisms contribute together to produce effective thermal conductivity. One possible way to account for the functionalized graphene is to consider the intrinsic thermal conductivities of graphene (κ_{g11}, κ_{g22}, κ_{g33}) and anatase (κ_2) and the corresponding thermal boundary resistances ($r_{1X}, r_{1Y}, r_{1Z}, r_2, r_{21}$) as variables that are dependent on the grafting densities g_{d1} and g_{d2}. Thus, the resulting set of functions including $\kappa_{g11}(g_{d1})$, $\kappa_{g22}(g_{d1})$, $\kappa_{g33}(g_{d1})$, $\kappa_2(g_{d2})$, $r_{1X}(g_{d1})$, $r_{1Y}(g_{d1})$, $r_{1Z}(g_{d1})$, $r_2(g_{d2})$, and $r_{21}(g_{d1}, g_{d2})$ should be prescribed. Very little information related to these functions is available. For example, κ_{g11} and r_1 were empirically related to g_{d1} for graphene nanoplatelets embedded in the polyamide-6,6 matrix [107], although the dependences look somewhat intricate.

It should also be noted that the synergetic effects of functionalization or assembling fillers can be more pronounced when the filler surfaces are subjected to preliminary purification. It is well known that different atomic and molecular impurities conjugated with filler surfaces have detrimental influences on the intrinsic and interfacial thermal properties of the filler [108–112]. In particular, the trace metallic and metalloid impurities [108], acidic residues [109], hydrocarbones [110], and even silicon [111] are ubiquitous on graphene surfaces.

In this study, no effort was undertaken to intentionally purify or functionalize the fillers, neither graphene nor anatase, because the main aim of this study is to reveal the thermal synergetic effects of assembling graphene and anatase. Therefore, we have no need to cater for laborious and time-consuming techniques for the purification surface of the fillers and the subsequent quantitative estimation of the type and amount of residual functional groups.

Finally, we compare the proposed model predictions and experimental results shown in Figure 1a. The open and closed triangles give the distributions of the calculated values of the thermal conductivity in our composites at different key parameters of the model. Varying the aspect ratio α from 0.005 to 0.02, the varying thermal boundary resistances r_2 and r_{21} from 10^{-5} to 10^{-10} $\mathrm{m^2{\cdot}W^{-1}{\cdot}K^{-1}}$, and varying the thicknesses of the interphase layers $h_1 = h_2$ from 10 to 30 nm yield a fair agreement of the calculated and experimental results. The bottom mesh of points (open triangles) characterizes the hypothetical situation of extremely small contact thermal resistances between the matrix and the fillers (minimum phonon exchange between the phases of the composite), whereas the upper mesh (closed triangles) corresponds to a strong interphase interaction with a significant overlap of the phonon density spectra of the fillers and the matrix. These calculations were performed in the soft spheres approximation (complete coverage of the surfaces of MLGs with TiO_2) for the complete self-assembling (at $p_1 = p_2 = 0$) of graphene and anatase in an epoxy polymer matrix. In this case, the variation in the TiO_2 diameter does not affect the calculation results. It is also important to note that the effect of incomplete coverage of the graphene surface with anatase (observed in Figure 4) on the calculated thermal conductivity is very small at the small numbers of filling particles C_1 and C_2 that were used in the experiments (last three paragraphs in Supplementary Note S1).

3. Materials and Methods

MLG nanoplatelets for our experiments were prepared from the flakes of thermally expanded graphite by using the electrochemical technique described by Xia et al. [113]. The structural properties of the nanoplatelets were tested by using X-ray diffraction (XRD) spectroscopy as described in our previous report [14]. A distinct difference between the XRD patterns of the initial graphite flakes and graphene sheets was observed [14]. Moreover, the Raman spectra of single-layer graphene particles and similarly fabricated samples of multilayer graphene particles were compared by Gorelov et al. [10], illustrating that our multilayer graphene nanoplatelets are composed of loosely bound graphene sheets. One can therefore suggest that the fabricated particles are multilayered graphene nanoplatelets rather than exfoliated graphite platelets.

To prevent the resulting MLG material from oxidizing, it was kept as the suspension. The particles were about 5×5 μm^2 in in-plane dimensions and 790 m^2/g in specific surface area. The value of the specific surface area was determined by measuring the amount of physically adsorbed nitrogen gas from adsorption–desorption isotherms according to the standard Brunauer, Emmett, and Teller (BET) method [114] by using an Autosorb Station 3 apparatus of Quantachrome Instruments (Boynton Beach, FL, USA).

The TiO_2-anatase nanoparticles were deposited on the MLG by adding them into the initial ethanol-based suspension of the MLG before its ultrasonic treatment. The specific surface area of the anatase particles was ~1500 m^2/g.

The commercially available CHS-EPOXY 520 (SpolChemie a.s., Usti nad Labem, Czech Republic) DGEBA-epoxy resin based on Bisphenol A diglycidyl ether (DGEBA), of epoxy group content (E-Index) 5.21–5.50 mol/kg, with an EEW (Epoxy Equivalent Weight) of 182–192 g/mol was used as the neat resin. Diethylenetriamine (abbreviated as Dien or DETA) was used as a curing agent. DETA is a nitrogen-containing organic compound with the formula $HN(CH_2CH_2NH_2)_2$ [115]. The epoxide to the hardener mass ratio was kept constant at 7:1. Details of the curing process can be found elsewhere [116].

The MLG mass loading values (C_1) for the nanocomposites were 0.5%, 1%, 2%, and 5%, whereas the TiO_2 mass loading values (C_2) were taken to be 0.5%, 1%, and 5%. To prepare the nanocomposites of the prescribed content (C_1, C_2), the following procedure was used: The epoxide olygomer to the hardener mass ratio (R_{OH}) was kept constant at 7:1, i.e., $R_{OH} = \frac{m_0}{m_h} = 7$. We hence started by taking the epoxide olygomer portion with the mass $m_0 = 105$ g poured out into a quartz glass. Then, we added the fillers in the following two steps: first, we added the 10% graphene–ethanol suspension portion with the graphene mass

$$m_g = \frac{C_1 m_e}{1 - C_1 - C_2} \tag{12}$$

and second, we added the dry anatase powder with the mass m_a given by

$$m_a = \frac{C_2 m_e}{1 - C_1 - C_2}, \tag{13}$$

where $m_e = m_0 + m_h = m_0 + \frac{1}{7} m_0 = 120$ g.

The as-prepared liquid composites were ultrasonically mixed until homogeneous suspensions were obtained. Then, they were stored in a vacuum chamber to remove ethanol and air bubbles. Finally, a hardener portion of $m_h = 15$ g was added to the treated compound, and the resultant mixture was mixed. After adding the hardener to the suspensions, their further polymerization occurred at room temperature for 72 h. Once again, the suspensions were stored in a vacuum for the first two hours at a reduced pressure of about 10^{-2} mbar to remove all the emerging gaseous constituents and thus prevent the formation of pores within the samples.

The morphology features of the nanocomposite were investigated with scanning electron microscopy (SEM) using a JEOL JSM-6490 microscope and with transmission electron microscopy (TEM) using a JEOL JEM-2100 microscope. Figure 9 shows the SEM

image of the TiO_2 particles decorating the graphene nanosheets (a), and TEM images of a hybrid graphene@anatase TiO_2 nanocomposite are shown in (b) and (c). It is seen in Figure 9a that the TiO_2 particles are well dispersed over the MLG surfaces. The high-resolution TEM image shown in Figure 9c displays a lattice fringe of about 0.33 nm, which can be attributed to the anatase (101) plane [117].

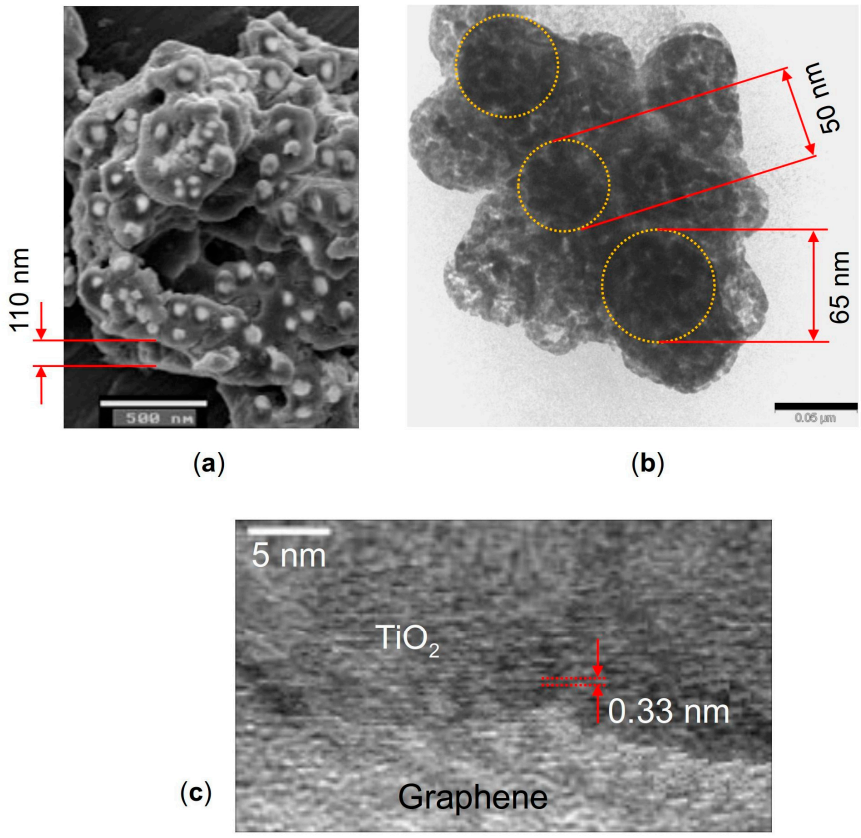


Figure 9. (**a**) SEM image of anatase TiO_2 particles decorating graphene nanosheets, (**b**) TEM image of the graphene flake with TiO_2 particles on it marked by dotted circles, and (**c**) high-resolution TEM image of a hybrid graphene flake@anatase TiO_2 nanocomposite. The scale bars are 500 nm in (**a**) and 50 nm in (**b**).

It was revealed by the microscopy that the TiO_2 particles have a diameter of ~30–70 nm, while the thickness of the MLG nanoplatelets ranges from about 30 to 150 nm. One needs to keep in mind that these dimensions are randomly distributed through irregular MLG@TiO_2 platelets. So, one needs to choose the values of the MLG and TiO_2 thicknesses (both are taken to be 50 nm above), and then obtain the numerical continuation solution branches in κ upon varying parameters. Some results describing varying κ_C upon varying MLG thickness are given in Supplementary Note S3.

Here, we used the two-probe measurement method to measure thermal conductivity [118]. Our automatic measuring system is schematically sketched in Figure 10. The sample was placed between two copper discs (heater and thermostat in Figure 10). An electric resistance served as a heater, and the power P released on it was determined with the electric current and voltage applied to the resistance. Additionally, the heat flux through the sample is $Q = P/S$, where S is the top and bottom surface area of the sample. A thermostat was used to keep the temperature of the top surface of the sample constant.

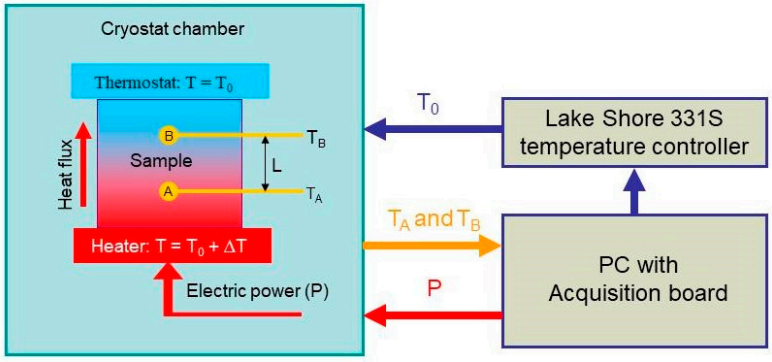


Figure 10. Schematics of the setup used for the thermal conductivity measurements. A and B are the temperature sensors embedded into the sample. L is the distance between the sensors. Thermostat is formed by mounting the top sample edge onto the cold head of the cryostat used (T-controlled heat sink).

By maintaining the stationary heat flux, one can write the following relation to evaluate the thermal conductivity [119]

$$\kappa = \frac{QL}{T_A - T_B}, \tag{14}$$

where L is the distance between the sensors, and T_A and T_B are the temperatures measured by sensors A and B, respectively.

The samples were cylindrically shaped with a diameter of 12.5 mm and a height of 6 mm. Two holes with diameters of 1 mm were drilled in the samples from the top and bottom surfaces to the center, in which the temperature sensors were placed (A and B in Figure 10). After that, the holes were filled with epoxy resin for better thermal contact between the sample and the temperature sensors. BAP64-02 NXP diodes were used as temperature sensors. The diodes had rather small dimensions of $1.2 \times 0.8 \times 0.6$ mm^3, which made it possible to place them inside the sample without difficulty.

We believe the diode temperature sensor was small enough to give rise to correct measurements since the ratio of the cross section of the sensor to that of the sample is less than 1%. There is little work reported on the usage of diode sensors to obtain thermal conductivity measurements of epoxy systems [120]. It may therefore be expected that the diode cannot lead itself to significantly interrupt the temperature field of the measurement.

Furthermore, the main channel of heat delivery to the pn junction is not its plastic cover, but rather the metal terminals to which the electrical lead wires are soldered. The thermal resistance to energy incoming from the junction to the soldering point is 85 K/W according to the diode performance specifications. Hence, though the diode is too big to be ignored and inevitably affects the characteristics of the temperature field, it is immediately obvious that the temperature sensor here is formed by the metal leads, which are completely immersed in the epoxy matrix. The surface area of the lead wires is comparable to the contact area of a thermocouple that is more commonly used to minimize the sensor influence. It is also obvious that the thermal resistance between the metal leads and epoxy resin will be more or less the same in both cases.

Moreover, temperature measurements are significantly affected by the thermal time constant. The thermal time constant of the system is the time required to come to within $1/e$ (≈37%) of the fixed value after a step thermal disturbance of the system [119]. The thermal time constant of the temperature sensor must be significantly less than the thermal time constant of the sample. Thus, the thermal resistance between the sensor and the sample will not significantly affect the measurement of the sample temperature. The thermal time constant of the diode is

$$\tau_t = R_t C_t, \tag{15}$$

where R_t is the resistance of the regions next to the junction, and $C_t = m_d C_d$ is the lumped thermal capacitance of the diode with the mass m_d and specific heat C_d. Taking $R_t = 85$ K/W given above and $C_d = 800$–1200 J·kg^{-1}·K^{-1} for the diode molding compound yields τ_t on the order of hundreds of ms in the worst case. Essentially, our measurements were carried out in a quasi-static regime such that, after setting the required temperature on the controller, the measuring system waited for dozens of minutes to achieve temperature stabilization. This waiting time depended on the temperature and was set to provide the rate of heating of the sample of less than 2 K/hour. This waiting time exceeded the thermal time constant of the diode. The sensors therefore did not appear to have an appreciable effect on the temperature measurements.

We also implemented a 2D finite element method (FEM) to model the temperature distribution using the COMSOL 5.3a and typical thermal conductivity parameters for diode materials, which are $\kappa = 400$ W/mK for copper and $\kappa = 0.58$–0.67 W/mK for the diode forming mass [121]. The simulation results are given in Figures 11 and 12. It is seen in Figure 11 that the temperature field around the diodes is not significantly distorted.

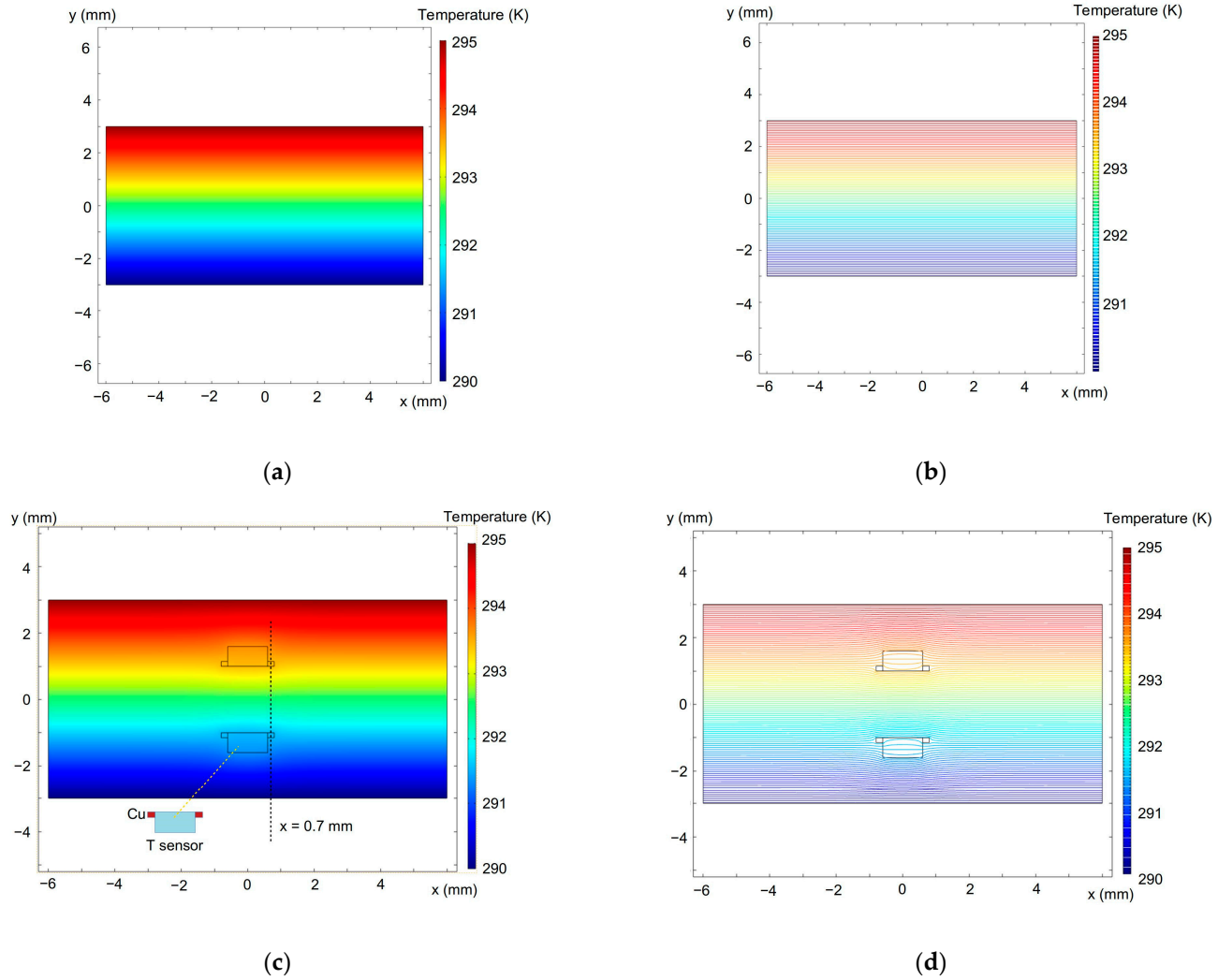


Figure 11. Simulated temperature distribution in the sample plane across the diode sensors in full color (left-hand images) and contour (right-hand images) plots. (**a**,**b**)—without the diodes; (**c**,**d**)—with the temperature sensors embedded into the sample (see Figure 10). The upper sample surface is heated. The dashed line at $x = 0.7$ mm in (**c**) shows the temperature distribution given in Figure 12.

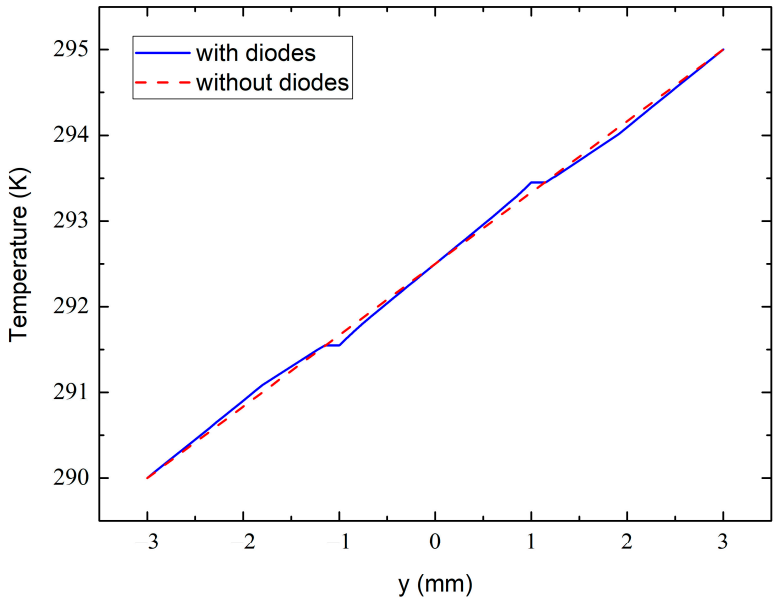


Figure 12. The temperature variation across the dashed line at $x = 0.7$ mm shown in Figure 11c with (solid line) and without (dashed line) the diode sensors.

The temperature variation across the dashed line at $x = 0.7$ mm in Figure 11c from the bottom to the top sample surface is shown in Figure 12. The dashed line simulates the variation in the absence of the diode sensors, whereas the solid line approximates the one with the embedded diodes. The dashed line in Figure 11c passes through the centers of the diode electrodes, which are heat-sensitive elements in our case. One can therefore see a perturbation in the temperature field at around $y \approx \pm 1$ mm just near the metal electrodes. This is due to the much higher thermal conductivity of the electrode than the epoxy resin. However, at the outer side of the electrodes (at $y \approx \pm 1.15$ mm in Figure 12), the solid- and dashed-line temperatures are practically identical. This ensures that the experimental temperature data obtained from these measurements are accurate and reliable when taking into account the thicknesses of the electrodes and when measuring the inter-sensor distance between their external edges.

Other factors to be taken into account when assessing the accuracy of the measurements are as follows: Copper wires with a thickness of 50 μm and a length of 100 mm were used to feed the diodes. Their thermal resistance is much higher than the thermal resistance of the sample, allowing for a heat leakage to be quenched. The epoxy resin without hardener was used to give a better thermal contact between the sample, heater, and cooler. A plastic screw defining a point contact constriction with a heat-insulating fastener was used to clamp the sample, which yielded a heat loss of less than 1%. With the above assumptions, the errors in the measured thermal conductivities do not exceed about 5%.

The sample was placed in a closed-cycle cryostat (CS204, Advanced Research Systems) that was used to vary its temperature. The temperature in the cryostat was controlled using a Lake Shore 331S controller through the computer's RS232 digital port. Measurements were carried out in the temperature range from 40 to 300 K.

4. Conclusions

A theoretical model based on the effective medium approximation was developed to calculate the loading dependence of the thermal conductivity κ in hybrid graphene–polymer nanocomposites and evaluate its sensitivity to the geometrical and material parameters of filling particles and the host polymer matrix, filler's mass concentration, self-assembling degree, and Kapitza thermal boundary resistances at emerging interfaces. The hybrid graphene@anatase nanosheets were modeled as sandwich-like structures of either parallelepiped- or spheroid-like configurations, where the geometrical and material

characteristics of the anatase layer were treated in a continuous media approximation for two extreme cases representing anatase nanoparticles as either soft or hard solid spheres. The differences between the model results obtained with the above two configurations increased with the decreasing the nanosheet's aspect ratio. The model was also capable of predicting the $\kappa(T)$ dependencies in the nanocomposites if the thermal parameters of the constituent phases and the thermal boundary resistances were known. The soft-sphere approach and related concept of the effective thickness allowed us to simplify the simulations and describe the interface thermal transport in the hybrid graphene@anatase nanosheets via the phenomenological thermal boundary resistance.

We also measured the temperature dependence of the thermal conductivity of epoxy nanocomposites filled with self-assembled hybrid nanoparticles composed of multilayered graphene nanoplatelets and anatase-TiO_2 nanoparticles within a temperature range from 40 K to 320 K. When the concentration of anatase in the composites increased, a saturation tendency in the $\kappa(T)$ dependence was observed above ≈150 K, which was possibly due to a saturation of the thermal conductivity of the anatase. A fair agreement between the calculated and measured room-temperature thermal conductivity was obtained.

The numerical results clearly illustrate the thermal screening effect of a low-conductive anatase layer that covers high-conductive graphene nanoplatelets. The observed growing thermal conductivity after raising the temperature is not only related to the increasing intrinsic thermal conductivities of both the fillers and host epoxy but is also subject to temperature-induced variations in the thermal boundary resistances.

An effective tailoring of κ is possible only if the anatase-to-graphene mass ratio does not exceed a certain bound, which corresponds to the sheer covering of graphene nanoplatelets by anatase nanoparticles. It is furthermore expected that κ will increase further when decreasing the thermal boundary resistances at the anatase–graphene interface. The latter can be realized by using more sophisticated techniques to chemically graft anatase to the graphene surface. However, when the concentration of hybrid nanosheets approaches its percolation thresholds with an increasing anatase-to-graphene concentration ratio, the temperature dependence of the composite's thermal conductivity weakens. It is therefore suggested that varying the filler concentration that covers the graphene nanoplatelets offers interesting opportunities of applied relevance in the area of self-assembling engineering of graphene surfaces.

Supplementary Materials: The following supporting information can be downloaded at https://www.mdpi.com/article/10.3390/molecules28217343/s1, Supplementary Note S1, Elaborating interphase regions; Supplementary Note S2, Volume concentrations of the constituents; Supplementary Note S3, Thermal conductivity upon varying graphene thickness. Refs. [122,123] are cited in Supplementary Materials.

Author Contributions: Conceptualization, O.K., B.M.G. and V.S.; methodology, A.B.N., O.I.P. and A.M.G.; software, O.I.P. and A.B.N.; validation, A.B.N., B.M.G., O.I.P. and A.M.G.; formal analysis, A.B.N., B.M.G., O.I.P., O.K. and V.S.; investigation, A.B.N. and A.M.G.; resources, O.K. and V.S.; data curation, O.I.P., B.M.G. and O.K.; writing—original draft preparation, O.I.P., B.M.G. and O.K.; writing—review and editing, O.K. and V.S.; visualization, A.M.G., O.I.P., O.K. and V.S.; supervision, B.M.G. and V.S.; project administration, O.K. and V.S.; funding acquisition, O.K. and V.S. All authors have read and agreed to the published version of the manuscript.

Funding: This research was supported by the Ministry of Education and Science of Ukraine, grant number 0122U001953. O.K. acknowledges the support from the Erwin Schrödinger Institute through the Special Research Fellow Programme.

Institutional Review Board Statement: Not applicable.

Informed Consent Statement: Not applicable.

Data Availability Statement: Data are contained within the article.

Conflicts of Interest: The authors declare no conflict of interest.

Nomenclature of the Model Parameters

L_X, L_Y, L_Z	linear dimensions of graphene nanoplatelets, nm
$\updownarrow_f$	filler particle size, nm
$\alpha = L_Z/L_X$	thickness-to-length aspect ratio of graphene nanoplatelets
R_2	average radius of anatase nanoparticles, nm
h_{int}	interphase layer thickness, nm
h_1	thickness of the graphene–epoxy interphase layer, nm
h_2	thickness of the anatase–epoxy interphase layer, nm
h_{21}	effective thickness of an anatase covering graphene nanoplatelets in the "soft-spheres" approximation, nm
κ_C	thermal conductivity of the composite
κ_m	intrinsic thermal conductivity of an epoxy matrix, $W{\cdot}m^{-1}{\cdot}K^{-1}$
κ_2 (κ_f)	intrinsic thermal conductivity of anatase nanoparticles (fillers), $W{\cdot}m^{-1}{\cdot}K^{-1}$
κ_{g11}, κ_{g22}, κ_{g33}	intrinsic in-plane (subscripts g11 and g22) and cross-plane (subscript g33) thermal conductivities of graphene nanoplatelets, $W{\cdot}m^{-1}{\cdot}K^{-1}$
$\kappa_{h,eff}$	effective thermal conductivity of the hybrid nanoparticle
$\kappa_{2,eff}$ ($\kappa_{f,eff}$)	effective thermal conductivity of anatase nanoparticles (fillers) embedded into epoxy ($\kappa_{f,eff} = \frac{\kappa_f}{1+(R_K\kappa_f)/\updownarrow_f} = \frac{\kappa_f}{1+\eta_f/\updownarrow_f}$), $W{\cdot}m^{-1}{\cdot}K^{-1}$
$\kappa_{g11,eff} = FK_{11}$, $\kappa_{g33,eff} = FK_{33}$	effective in-plane and cross-plane thermal conductivities of graphene nanoplatelets embedded into epoxy, $W{\cdot}m^{-1}{\cdot}K^{-1}$
κ_{int}	thermal conductivity of interphase regions ($\kappa_{int} = h_{int}/2R_K$), $W{\cdot}m^{-1}{\cdot}K^{-1}$
Kb_1	thermal conductivity of the graphene–epoxy interphase layer, $W{\cdot}m^{-1}{\cdot}K^{-1}$
Kb_2	thermal conductivity of the anatase–epoxy interphase layer, $W{\cdot}m^{-1}{\cdot}K^{-1}$
Kb_{21}	effective thermal conductivity of the anatase layer covering the graphene nanoplatelet, $W{\cdot}m^{-1}{\cdot}K^{-1}$
R_K (R_{K1} and R_{K2})	Kapitza resistance (at MLG-TiO_2 and TiO_2-epoxy interfaces), $W^{-1}{\cdot}m^2{\cdot}K$
r_1	effective Kapitza thermal boundary resistance of the graphene–epoxy interface, $W^{-1}{\cdot}m^2{\cdot}K$
r_{1X}, r_{1Y}	in-plane Kapitza thermal boundary resistance of the graphene–epoxy interface, $W^{-1}{\cdot}m^2{\cdot}K$
r_{1Z}	cross-plane Kapitza thermal boundary resistance of the graphene–epoxy interface, $W^{-1}{\cdot}m^2{\cdot}K$
r_{1av}	averaged Kapitza thermal boundary resistance of the graphene–epoxy interface, $W^{-1}{\cdot}m^2{\cdot}K$
r_2	Kapitza thermal boundary resistance of the anatase–epoxy interface, $W^{-1}{\cdot}m^2{\cdot}K$
r_{21}	Kapitza thermal boundary resistance of the graphene–anatase interface, $W^{-1}{\cdot}m^2{\cdot}K$
$\eta_{m,f} = R_K\,\kappa_{m,f}$	Kapitza length (subscript $m-$ matrix, $f-$ filler), nm
C_1	mass concentration of graphene nanoplatelets in the composite
C_2	mass concentration of anatase nanoparticles in the composite
φ_n	volume concentration of constituent phases (subscripts $n = 0$, 1, 2, and 3 correspond to the polymer matrix, free MLG nanoplatelets, free anatase nanoparticles, and hybrid MLG@anatase nanoparticles, respectively); see Equations (S39)–(S45) (Supplementary Note S2)
φ_{i1}	volume portion of the graphene–epoxy interphase layer
φ_{i2}	volume portion of the anatase–epoxy interphase layer
φ_{i3}	volume portion of the interphase layer surrounding graphene@anatase hybrid nanoparticles

φ_{i30}	volume portion of an anatase in graphene@anatase hybrid nanoparticles
Φ_n	functions defined by Equations (S1)–(S4) (Supplementary Note S1)
$F_{1,2,3}$	volume factors, which determine the ratio of the interphase layer's volume to the particle's volume
$p_{1,2}$	mass portions of free (unassembled) fillers, graphene (subscript 1), and anatase (subscript 2)
ρ_n	mass densities of the polymer matrix ($n = 0$), graphene nanoplatelets ($n = 1$), and anatase nanoparticles ($n = 2$), kg·m^{-3}
$\rho_{i1,2}$	mass densities of the graphene–epoxy (subscript 1) and anatase–epoxy (subscript 2) interphase layers
m_n, v_n, s_n	masses (in kg), volumes (in m^3), and surface areas (in m^2) of graphene nanoplatelets ($n = 1$) and anatase nanoparticles ($n = 2$)
$S_{ij}(\alpha)$	two-rank Eshelby tensor
N_{21}	total number of anatase nanoparticles per single graphene nanoplatelet
N_0	maximum number of anatase nanoparticles that can be packed tightly over the surface of a single graphene nanoplatelet
NL_2	hypothetical number of layers of anatase particles covering graphene nanoplatelets
$H_{21,eff}$	effective thickness of an anatase covering graphene nanoplatelets in the "hard-spheres" approximation, nm
R_G	radius of gyration of the polymer matrix
g_d	grafting density

References

1. Wang, M.C.; Lai, Z.B.; Galpaya, D.; Yan, C.; Hu, N.; Zhou, L.M. Atomistic simulation of surface functionalization on the interfacial properties of graphene-polymer nanocomposites. *J. Appl. Phys.* **2014**, *115*, 123520. [CrossRef]
2. Monteserín, C.; Blanco, M.; Aranzabe, E.; Aranzabe, A.; Vilas, J.L. Effects of graphene oxide and chemically reduced graphene oxide on the curing kinetics of epoxy amine composites. *J. Appl. Polym.* **2017**, *134*, 44803. [CrossRef]
3. Vryonis, O.; Virtanen, S.T.H.; Andritsch, T.; Vaughan, A.S.; Lewin, P.L. Understanding the cross-linking reactions in highly oxidized graphene/epoxy nanocomposite systems. *J. Mater. Sci.* **2018**, *54*, 3035–3051. [CrossRef]
4. Nadtochiy, A.; Gorelov, B.; Polovina, O.; Shulga, S.; Korotchenkov, O. Probing matrix/filler interphase with ultrasonic waves. *J. Mater. Sci.* **2021**, *56*, 14047–14069. [CrossRef]
5. Katti, P.; Kundan, K.V.; Kumar, S.; Bose, S. Improved mechanical properties through engineering the interface by poly (ether ether ketone) grafted graphene oxide in epoxy based nanocomposites. *Polymer* **2017**, *122*, 184–193. [CrossRef]
6. Li, M.; Zhou, H.; Zhang, Y.; Liao, Y.; Zhou, H. The effect of defects on the interfacial mechanical properties of graphene/epoxy composites. *RSC Adv.* **2017**, *7*, 46101–46108. [CrossRef]
7. Rafiee, R.; Eskandariyun, A. Estimating Young's modulus of graphene/polymer composites using stochastic multi-scale modeling. *Compos. B Eng.* **2019**, *173*, 106842. [CrossRef]
8. Zhang, S.; Zhang, H.; Feng, H.; Yan, J.; Liu, P.; Peng, Z. Relaxation processes and conduction mechanism of epoxy resin filled with graphene oxide. *IEEE Trans. Dielectr. Electr. Insul.* **2017**, *24*, 519–527. [CrossRef]
9. Ravindran, A.; Feng, C.; Huang, S.; Wang, Y.; Zhao, Z.; Yang, J. Effects of graphene nanoplatelet size and surface area on the ac electrical conductivity and dielectric constant of epoxy nanocomposites. *Polymers* **2018**, *10*, 477. [CrossRef] [PubMed]
10. Gorelov, B.M.; Mischanchuk, O.V.; Sigareva, N.V.; Shulga, S.V.; Gorb, A.M.; Polovina, O.I.; Yukhymchuk, V.O. Structural and dipole-relaxation processes in epoxy-multilayer graphene composites with low filler content. *Polymers* **2021**, *13*, 3360. [CrossRef] [PubMed]
11. Shen, X.; Wang, Z.; Wu, Y.; Liu, X.; He, Y.-B.; Kim, J.-K. Multilayer graphene enables higher efficiency in improving thermal conductivities of graphene/epoxy composites. *Nano Lett.* **2016**, *16*, 3585–3593. [CrossRef]
12. Su, Y.; Li, J.J.; Weng, G.J. Theory of thermal conductivity of graphene-polymer nanocomposites with interfacial Kapitza resistance and graphene-graphene contact resistance. *Carbon* **2018**, *137*, 222–233. [CrossRef]
13. Xiao, W.; Zhai, X.; Ma, P.; Fan, T.; Li, X. Numerical study on the thermal behavior of graphene nanoplatelets/epoxy composites. *Results Phys.* **2018**, *9*, 673–679. [CrossRef]
14. Gorelov, B.M.; Gorb, A.M.; Nadtochiy, A.; Starokadomskiy, D.L.; Kuryliuk, V.V.; Sigareva, N.V.; Shulga, S.V.; Ogenko, V.M.; Korotchenkov, O.O.; Polovina, O.I. Epoxy filled with bare and oxidized multi-layered graphene nanoplatelets: A comparative study of filler loading impact on thermal properties. *J. Mater. Sci.* **2019**, *54*, 9247–9266. [CrossRef]
15. Zhang, P.; Zeng, J.; Zhai, S.; Xian, Y.; Yang, D.; Li, Q. Thermal properties of graphene filled polymer composite thermal interface materials. *Macromol. Mater. Eng.* **2017**, *302*, 1700068. [CrossRef]
16. Lewis, J.S.; Perrier, T.; Barani, Z.; Kargar, F.; Balandin, A.A. Thermal interface materials with graphene fillers: Review of the state of the art and outlook for future applications. *Nanotechnology* **2021**, *32*, 142003. [CrossRef]

17. Ma, H.; Gao, B.; Wang, M.; Yuan, Z.; Shen, J.; Zhao, J. Strategies for enhancing thermal conductivity of polymer-based thermal interface materials: A review. *J. Mater. Sci.* **2021**, *56*, 1064–1086. [CrossRef]
18. El-Kady, M.F.; Shao, Y.; Kaner, R.B. Graphene for batteries, supercapacitors and beyond. *Nat. Rev. Mater.* **2016**, *1*, 16033. [CrossRef]
19. Liu, Y.; Zhou, G.; Liu, K.; Cui, Y. Design of complex nanomaterials for energy storage: Past success and future opportunity. *Acc. Chem. Res.* **2017**, *50*, 2895–2905. [CrossRef] [PubMed]
20. Al-Saleh, M. Carbon-based polymer nanocomposites as dielectric energy storage materials. *Nanotechnology* **2018**, *30*, 062001. [CrossRef] [PubMed]
21. Shao, Y.; El-Kady, M.F.; Wang, L.J.; Zhang, Q.; Li, Y.; Wang, H.; Mousavi, M.F.; Kaner, R.B. Graphene-based materials for flexible supercapacitors. *Chem. Soc. Rev.* **2015**, *44*, 3639–3665. [CrossRef]
22. Azman, N.H.N.; Nazir, S.M.M.; Ngee, L.H.; Sulaiman, Y. Graphene-based ternary composites for supercapacitors. *Int. J. Energy Res.* **2018**, *42*, 2104–2116. [CrossRef]
23. Ishaq, S.; Moussa, M.; Kanwal, F.; Ehsan, M.; Saleem, M.; Van, T.N.; Losic, D. Facile synthesis of ternary graphene nanocomposites with doped metal oxide and conductive polymers as electrode materials for high performance supercapacitors. *Sci. Rep.* **2019**, *9*, 5974. [CrossRef]
24. Movil, O.; Frank, L.; Staser, J.A. Graphene oxide–polymer nanocomposite anion-exchange membranes. *J. Electrochem. Soc.* **2015**, *162*, F419–F426. [CrossRef]
25. Luo, Z.; Gong, Y.; Liao, X.; Pan, Y.; Zhang, H. Nanocomposite membranes modified by graphene-based materials for anion exchange membrane fuel cells. *RSC Adv.* **2016**, *6*, 13618–13625. [CrossRef]
26. Pandey, R.P.; Shukla, G.; Manohar, M.; Shahi, V.K. Graphene oxide based nanohybrid proton exchange membranes for fuel cell applications: An overview. *Adv. Colloid Interface Sci.* **2017**, *240*, 15–30. [CrossRef]
27. Alabi, A.; Cseri, L.; Al Hajaj, A.; Szekely, G.; Budd, P.; Zou, L. Electrostatically-coupled graphene oxide nanocomposite cation exchange membrane. *J. Membr. Sci.* **2019**, *594*, 117457. [CrossRef]
28. Yadav, R.; Subhash, A.; Chemmenchery, N.; Kandasubramanian, B. Graphene and graphene oxide for fuel cell technology. *Ind. Eng. Chem. Res.* **2018**, *57*, 9333–9350. [CrossRef]
29. Wang, C.; Wang, Y.; Yang, Z.; Hu, N. Review of recent progress on graphene-based composite gas sensors. *Ceram. Int.* **2021**, *47*, 16367–16384. [CrossRef]
30. Chakraborthy, A.; Nuthalapati, S.; Nag, A.; Afsarimanesh, N.; Alahi, M.E.E.; Altinsoy, M.E. A critical review of the use of graphene-based gas sensors. *Chemosensors* **2022**, *10*, 355. [CrossRef]
31. Anderson, L.; Govindaraj, P.; Ang, A.; Mirabedini, A.; Hameed, N. Modelling, fabrication and characterization of graphene/polymer nanocomposites for electromagnetic interference shielding applications. *Carbon Trends* **2021**, *4*, 100047. [CrossRef]
32. Tan, X.; Yuan, Q.; Qiu, M.; Yu, J.; Jiang, N.; Lin, C.-T.; Dai, W. Rational design of graphene/polymer composites with excellent electromagnetic interference shielding effectiveness and high thermal conductivity: A mini review. *J. Mater. Sci. Technol.* **2022**, *117*, 238–250. [CrossRef]
33. Panahi-Sarmad, M.; Noroozi, M.; Xiao, X.; Park, C.B. Recent advances in graphene-based polymer nanocomposites and foams for electromagnetic interference shielding applications. *Ind. Eng. Chem. Res.* **2022**, *61*, 1545–1568. [CrossRef]
34. Rohini, R.; Katti, P.; Bose, S. Tailoring the interface in graphene/thermoset polymer composites: A critical review. *Polymer* **2015**, *70*, A17–A34. [CrossRef]
35. Atif, R.; Shyha, I.; Inam, F. Mechanical, thermal, and electrical properties of graphene-epoxy nanocomposites—A review. *Polymers* **2016**, *8*, 281. [CrossRef] [PubMed]
36. Atif, R.; Inam, F. Modeling and simulation of graphene based polymer nanocomposites: Advances in the last decade. *Graphene* **2016**, *5*, 96–142. [CrossRef]
37. Mohan, V.B.; Lau, K.T.; Hui, D.; Bhattacharyya, D. Graphene-based materials and their composites: A review on production, applications and product limitations. *Compos. B. Eng.* **2018**, *142*, 200–220. [CrossRef]
38. Szeluga, U.; Pusz, S.; Kumanek, B.; Olszowska, K.; Kobyliukh, A.; Trzebicka, B. Effect of graphene filler structure on electrical, thermal, mechanical, and fire retardant properties of epoxy-graphene nanocomposites—A review. *Crit. Rev. Solid State Mater. Sci.* **2021**, *46*, 152–187. [CrossRef]
39. Siwal, S.S.; Zhang, Q.; Devi, N.; Thakur, V.K. Review: Carbon-based polymer nanocomposite for high-performance energy storage applications. *Polymers* **2020**, *12*, 505. [CrossRef]
40. Dubey, R.; Guruviah, V. Review of carbon-based electrode materials for supercapacitor energy storage. *Ionics* **2019**, *25*, 1419–1445. [CrossRef]
41. Luo, H.; Zhou, X.; Ellingford, C.; Zhang, Y.; Chen, S.; Zhou, K.; Zhang, D.; Bowen, C.R.; Wan, C. Interface design for high energy density polymer nanocomposites. *Chem. Soc. Rev.* **2019**, *48*, 4424–4465. [CrossRef] [PubMed]
42. Wu, Z.-S.; Zhou, G.; Yin, L.-C.; Ren, W.; Li, F.; Cheng, H.-M. Graphene/metal oxide composite electrode materials for energy storage. *Nano Energy* **2012**, *1*, 107–131. [CrossRef]
43. Farooq, U.; Ahmed, F.; Pervez, S.A.; Rehman, S.; Pope, M.A.; Fichtner, M.; Roberts, E.P.L. A stable TiO_2–graphene nanocomposite anode with high rate capability for lithium-ion batteries. *RSC Adv.* **2020**, *10*, 29975–29982. [CrossRef]
44. Tang, B.; Chen, H.; Peng, H.; Wang, Z.; Huang, W. Graphene modified TiO_2 composite photocatalysts: Mechanism, progress and perspective. *Nanomaterials* **2018**, *8*, 105. [CrossRef] [PubMed]

45. Martins, P.M.; Ferreira, C.G.; Silva, A.R.; Magalhães, B.; Alves, M.M.; Pereira, L.; Marques, P.A.A.P.; Melle-Franco, M.; Lanceros-Méndez, S. TiO_2/graphene and TiO_2/graphene oxide nanocomposites for photocatalytic applications: A computer modeling and experimental study. *Compos. B Eng.* **2018**, *145*, 39–46. [CrossRef]
46. Sagadevan, S.; Lett, J.A.; Weldegebrieal, G.K.; Biswas, M.R.D.; Oh, W.C.; Alshahateet, S.F.; Fatimah, I.; Mohammad, F.; Al-Lohedan, H.A.; Paiman, S.; et al. Enhanced gas sensing and photocatalytic activity of reduced graphene oxide loaded TiO_2 nanoparticles. *Chem. Phys. Lett.* **2021**, *780*, 138897. [CrossRef]
47. Siwachi, B.; Mohan, D.; Sharma, S.; Jyoti, D. Process optimization of dye-sensitized solar cells using TiO_2–graphene nanocomposites. *Bull. Mater. Sci.* **2017**, *40*, 1371–1377. [CrossRef]
48. Kusiak-Nejman, E.; Morawski, A.W. TiO_2/graphene-based nanocomposites for water treatment: A brief overview of charge carrier transfer, antimicrobial and photocatalytic performance. *Appl. Catal. B Environ.* **2019**, *253*, 179–186. [CrossRef]
49. Simari, C.; Lufrano, E.; Godbert, N.; Gournis, D.; Coppola, L.; Nicotera, I. Titanium dioxide grafted on graphene oxide: Hybrid nanofiller for effective and low-cost proton exchange membranes. *Nanomaterials* **2020**, *10*, 1572. [CrossRef]
50. Diebold, U. The surface science of titanium dioxide. *Surf. Sci. Rep.* **2003**, *48*, 53–229. [CrossRef]
51. Thompson, T.L.; Yates, J.T. Surface science studies of the photoactivation of TiO_2—New photochemical processes. *Chem. Rev.* **2006**, *106*, 4428–4453. [CrossRef]
52. Chen, X.; Mao, S.S. Titanium dioxide nanomaterials: Synthesis, properties, modifications, and applications. *Chem. Rev.* **2007**, *107*, 2891–2959. [CrossRef] [PubMed]
53. Nowotny, M.K.; Sheppard, L.R.; Bak, T.; Nowotny, J. Defect chemistry of titanium dioxide. Application of defect engineering in processing of TiO_2-based photocatalysts. *J. Phys. Chem. C* **2008**, *112*, 5275–5300. [CrossRef]
54. Angelis, F.D.; Valentin, C.D.; Fantacci, S.; Vittadini, A.; Selloni, A. Theoretical studies on anatase and less common TiO_2 phases: Bulk, surfaces, and nanomaterials. *Chem. Rev.* **2014**, *114*, 9708–9753. [CrossRef] [PubMed]
55. Kusiak-Nejman, E.; Wanag, A.; Kowalczyk, Ł.; Kapica-Kozar, J.; Colbeau-Justin, C.; Mendez Medrano, M.G.; Morawski, A.W. Graphene-oxide TiO_2 and reduced graphene oxide-TiO_2 nanocomposites: Insight in charge-carrier lifetime measurements. *Catal. Today* **2017**, *287*, 189–195. [CrossRef]
56. Yadav, A.; Yadav, M.; Gupta, S.; Popat, Y.; Gangan, A.; Chakraborty, B.; Ramaniah, L.M.; Fernandes, R.; Miotello, A.; Press, M.R.; et al. Effect of graphene oxide loading on TiO_2: Morphological, optical, interfacial charge dynamics—A combined experimental and theoretical study. *Carbon* **2019**, *143*, 51–62. [CrossRef]
57. Heo, U.S.; Kim, D.-W.; Kim, K.-S.; Park, D.-W. A facile synthesis of anatase TiO_2-Graphene nanocomposites using plasma and heat treatment. *Appl. Surf. Sci.* **2019**, *474*, 118–126. [CrossRef]
58. Cui, W.; Du, F.; Zhao, J.; Zhang, W.; Yang, Y.; Xie, X.; Mai, Y.-W. Improving thermal conductivity while retaining high electrical resistivity of epoxy composites by incorporating silica-coated multi-walled carbon nanotubes. *Carbon* **2010**, *49*, 495–500. [CrossRef]
59. Im, H.; Hwang, Y.; Moon, J.H.; Lee, S.H.; Kim, J. The thermal conductivity of $Al(OH)_3$ covered MWCNT/epoxy terminated dimethyl polysiloxane composite based on analytical $Al(OH)_3$ covered MWCNT. *Compos. A Appl. Sci. Manuf.* **2013**, *54*, 159–165. [CrossRef]
60. Peierls, R.E. *Quantum Theory of Solids*; Oxford University Press: London, UK, 1955.
61. Pierson, H.O. *Handbook of Carbon, Graphite, Diamonds and Fullerenes: Processing, Properties and Applications*; Noyes Publications: Norwich, NJ, USA, 2010.
62. Balandin, A. Thermal properties of graphene and nanostructured carbon materials. *Nat. Mater.* **2011**, *10*, 569–581. [CrossRef]
63. Burger, N.; Laachachi, A.; Ferriol, M.; Lutz, M.; Toniazzo, V.; Ruch, D. Review of thermal conductivity in composites: Mechanisms, parameters and theory. *Prog. Polym. Sci.* **2016**, *61*, 1–28. [CrossRef]
64. Kuryliuk, V.; Nadtochiy, A.; Korotchenkov, O.; Wang, C.C.; Li, P.W. A model for predicting the thermal conductivity of SiO_2–Ge nanoparticle composites. *Phys. Chem. Chem. Phys.* **2015**, *17*, 13429–13441. [CrossRef]
65. Goodson, K.E.; Su, L.T.; Antoniadis, D.A.; Flik, M.I. Prediction and measurement of the thermal conductivity of amorphous dielectric layers. *J. Heat Transfer* **1994**, *116*, 317–324. [CrossRef]
66. Zeller, R.C.; Pohl, R.O. Thermal conductivity and specific heat of noncrystalline solids. *Phys. Rev. B* **1971**, *4*, 2029–2041. [CrossRef]
67. Anderson, P.W.; Halperin, B.I.; Varma, M.M. Anomalous low-temperature thermal properties of glasses and spin glasses. *Philos. Mag.* **1972**, *25*, 1–9. [CrossRef]
68. Phillips, W.A. Tunneling states in amorphous solids. *J. Low Temp. Phys.* **1972**, *7*, 351–360. [CrossRef]
69. Galperin, Y.M.; Karpov, V.G.; Kozub, V.I. Localized states in glasses. *Adv. Phys.* **1989**, *38*, 669–737. [CrossRef]
70. Parshin, D.A. Interactions of soft atomic potentials and universality of low-temperature properties of glasses. *Phys. Rev. B* **1994**, *49*, 9400–9418. [CrossRef] [PubMed]
71. Grayson, M.; Eckroth, D. *Encyclopedia of Chemical Technology*, 3rd ed.; Wiley: Hoboken, NJ, USA, 1982.
72. Available online: https://rruff.info/doclib/hom/anatase.pdf (accessed on 24 October 2023).
73. Gresil, M.; Wang, Z.; Poutrel, Q.-A.; Soutis, C. Thermal diffusivity mapping of graphene based polymer nanocomposites. *Sci. Rep.* **2017**, *7*, 5536. [CrossRef]
74. Available online: http://webmineral.com/data/Anatase.shtml#.ZDwjK3ZByUk (accessed on 24 October 2023).
75. Cabaleiro, D.; Nimo, J.; Pastoriza-Gallego, M.J.; Piceiro, M.M.; Legido, J.L.; Lugo, L. Thermal conductivity of dry anatase and rutile nano-powders and ethylene and propylene glycol-based TiO_2 nanofluids. *J. Chem. Thermodyn.* **2015**, *83*, 67–76. [CrossRef]

76. Shahil, K.M.F.; Balandin, A.A. Graphene−multilayer graphene nanocomposites as highly efficient thermal interface materials. *Nano Lett.* **2012**, *12*, 861–867. [CrossRef] [PubMed]
77. Evans, W.; Prasher, R.; Fish, J.; Meakin, P.; Phelan, P.; Keblinski, P. Effect of aggregation and interfacial thermal resistance on thermal conductivity of nanocomposites and colloidal nanofluids. *Int. J. Heat Mass Transf.* **2008**, *51*, 1431–1438. [CrossRef]
78. Bolis, V.; Busco, C.; Ciarletta, M.; Distasi, C.; Erriquez, J.; Fenoglio, I.; Livraghi, S.; Morel, S. Hydrophilic/hydrophobic features of TiO_2 nanoparticles as a function of crystal phase, surface area and coating, in relation to their potential toxicity in peripheral nervous system. *J. Colloid Interface Sci.* **2012**, *369*, 28–39. [CrossRef]
79. ter Haar, D. (Ed.) *Collected Papers of P. L. Kapitza*; Pergamon: Oxford, UK, 1965; Volume 2, p. 581.
80. Roy, A.K.; Farmer, B.L.; Varshney, V.; Sihn, S.; Lee, J.; Ganguli, S. Importance of interfaces in governing thermal transport in composite materials: Modeling and experimental perspectives. *ACS Appl. Mater. Interfaces* **2012**, *4*, 545–563. [CrossRef] [PubMed]
81. Kelham, S.; Rosenberg, H. Phonon scattering and the linear specific heat term in epoxy-resins at low temperatures. *J. Phys. Colloq.* **1978**, *39*, 982–983. [CrossRef]
82. Garrett, K.W.; Rosenberg, H.M. The thermal conductivity of epoxy-resin / powder composite materials. *J. Phys. D Appl. Phys.* **1974**, *7*, 1247–1258. [CrossRef]
83. Muñoz, E.; Lu, J.; Yakobson, B.I. Ballistic thermal conductance of graphene ribbons. *Nano Lett.* **2010**, *10*, 1652–1656. [CrossRef]
84. Mingo, N.; Broido, D. Carbon nanotube ballistic thermal conductance and its limits. *Phys. Rev. Lett.* **2005**, *95*, 096105. [CrossRef]
85. Cahill, D.G.; Ford, W.K.; Goodson, K.E.; Mahan, G.D.; Majumdar, A.; Maris, H.J.; Merlin, R.; Phillpot, R.S.R. Nanoscale thermal transport. *J. Appl. Phys.* **2003**, *93*, 793818. [CrossRef]
86. Torres, P.; Rurali, R. Thermal conductivity of rutile and anatase TiO_2 from first principles. *J. Phys. Chem. C* **2019**, *123*, 30851–30855. [CrossRef]
87. Mettan, X.; Jaćimović, J.; Barišić, O.S.; Pisoni, A.; Batistić, I.; Horváth, E.; Brown, S.; Rossi, L.; Szirmai, P.; Farkas, B.; et al. Tailoring thermal conduction in anatase TiO_2. *Commun. Phys.* **2019**, *2*, 123. [CrossRef]
88. Swartz, E.T.; Pohl, R.O. Thermal boundary resistance. *Rev. Mod. Phys.* **1989**, *61*, 605–668. [CrossRef]
89. Chen, G. Thermal conductivity and ballistic-phonon transport in the cross-plane direction of superlattices. *Phys. Rev. B* **1998**, *57*, 14958–14973. [CrossRef]
90. Prasher, R.S.; Phelan, P.E. Microscopic and macroscopic thermal contact resistances of pressed mechanical contacts. *J. Appl. Phys.* **2006**, *100*, 063538. [CrossRef]
91. Yang, S.B.; Feng, X.L.; Müllen, K. Sandwich-Like, graphene-based titania nanosheets with high surface area for fast lithium storage. *Adv. Mater.* **2011**, *23*, 3575–3579. [CrossRef]
92. Zheng, Q.; Braun, P.V.; Cahill, D.G. Thermal conductivity of graphite thin films grown by low temperature chemical vapor deposition on Ni (111). *Adv. Mater. Interfaces* **2016**, *3*, 1600234. [CrossRef]
93. Wu, W.; Yang, H.; Liu, Y.; Yang, S.; Yang, P. Effect of defects on heat transfer at the graphene/epoxy interface. *Int. Commun. Heat Mass Transf.* **2022**, *131*, 105846. [CrossRef]
94. Wang, Y.; Yang, C.; Pei, Q.-X.; Zhang, Y. Some aspects of thermal transport across the interface between graphene and epoxy in nanocomposites. *ACS Appl. Mater. Interfaces* **2016**, *8*, 8272–8279. [CrossRef]
95. Ndoro, T.V.M.; Böhm, M.C.; Müller-Plathe, F. Interface and interphase dynamics of polystyrene chains near grafted and ungrafted silica nanoparticles. *Macromolecules* **2011**, *45*, 171–179. [CrossRef]
96. Eslami, H.; Rahimi, M.; Müller-Plathe, F. Molecular dynamics simulation of a silica nanoparticle in oligomeric poly(methyl methacrylate): A model system for studying the interphase thickness in a polymer−nanocomposite via different properties. *Macromolecules* **2013**, *46*, 8680–8692. [CrossRef]
97. Park, H.; Chung, I.; Cho, M. Effect of molecular structure of curing agents on cyclic creep in highly cross-linked epoxy polymers. *J. Polym. Sci.* **2020**, *58*, 1617–1631. [CrossRef]
98. Odegard, G.M.; Clancy, T.C.; Gates, T.S. Modeling of the mechanical properties of nanoparticle/polymer composites. *Polymer* **2005**, *46*, 553–562. [CrossRef]
99. Pitsa, D.; Danikas, M.G. Interfaces features in polymer nanocomposites: A review of proposed models. *Nano* **2011**, *6*, 497–508. [CrossRef]
100. Wang, Y.; Shan, J.W.; Weng, G.J. Percolation threshold and electrical conductivity of graphene-based nanocomposites with filler agglomeration and interfacial tunneling. *J. Appl. Phys.* **2015**, *118*, 06161. [CrossRef]
101. Nan, C.-W.; Birringer, R.; Clarke, D.R.; Gleiter, H. Effective thermal conductivity of particulate composites with interfacial thermal resistance. *J. Appl. Phys.* **1997**, *81*, 6692–6699. [CrossRef]
102. Kuilla, T.; Bhadra, S.; Yao, D.; Kim, N.H.; Bose, S.; Lee, J.H. Recent advances in graphene based polymer composites. *Prog. Polym. Sci.* **2010**, *35*, 1350–1375. [CrossRef]
103. Punetha, V.D.; Rana, S.; Yoo, H.J.; Chaurasia, A.; McLeskey, J.T.; Ramasamy, M.S.; Sahoo, N.G.; Cho, J.W. Functionalization of carbon nanomaterials for advanced polymer nanocomposites: A comparison study between CNT and graphene. *Prog. Polym. Sci.* **2017**, *67*, 1–47. [CrossRef]
104. Dreyer, D.R.; Park, S.; Bielawski, C.W.; Ruoff, R.S. The chemistry of graphene oxide. *Chem. Soc. Rev.* **2009**, *39*, 228–240. [CrossRef]
105. Choi, E.-Y.; Han, T.H.; Hong, J.; Kim, J.E.; Lee, S.H.; Kim, H.W.; Kim, S.O. Noncovalent functionalization of graphene with end-functional polymers. *J. Mater. Chem.* **2010**, *20*, 1907–1912. [CrossRef]

106. Tarannum, F.; Muthaiah, R.; Danayat, S.; Foley, K.; Annam, R.S.; Walters, K.B.; Garg, J. Chemically edge-carboxylated graphene enhances the thermal conductivity of polyetherimide–graphene nanocomposites. *ACS Appl. Mater. Interfaces* **2022**, *14*, 14753–14763. [CrossRef]
107. Gao, Y.; Müller-Plathe, F. Increasing the thermal conductivity of graphene-polyamide-6,6 nanocomposites by surface-grafted polymer chains: Calculation with molecular dynamics and effective-medium approximation. *J. Phys. Chem. B* **2016**, *120*, 1336–1346. [CrossRef] [PubMed]
108. Wong, C.H.A.; Sofer, Z.; Kubešová, M.; Kučera, J.; Matějková, S.; Pumera, M. Synthetic routes contaminate graphene materials with a whole spectrum of unanticipated metallic elements. *Proc. Natl. Acad. Sci. USA* **2014**, *111*, 13774–13779. [CrossRef] [PubMed]
109. Barbolina, I.; Woods, C.R.; Lozano, N.; Kostarelos, K.; Novoselov, K.S.; Roberts, I.S. Purity of graphene oxide determines its antibacterial activity. *2D Mater.* **2016**, *3*, 025025. [CrossRef]
110. Kozbial, A.; Zhou, F.; Li, Z.; Liu, H.; Li, L. Are graphitic surfaces hydrophobic? *Acc. Chem. Res.* **2016**, *49*, 2765–2773. [CrossRef]
111. Jalili, R.; Esrafilzadeh, D.; Aboutalebi, S.H.; Sabri, Y.M.; Kandjani, A.E.; Bhargava, S.K.; Della Gaspera, E.; Gengenbach, T.R.; Walker, A.; Chao, Y.; et al. Silicon as a ubiquitous contaminant in graphene derivatives with significant impact on device performance. *Nat. Commun.* **2018**, *9*, 5070. [CrossRef]
112. Pumera, M.; Ambrosi, A.; Chng, E.L.K. Impurities in graphenes and carbon nanotubes and their influence on the redox properties. *Chem. Sci.* **2012**, *3*, 3347–3355. [CrossRef]
113. Xia, Z.Y.; Pezzini, S.; Treossi, E.; Giambastiani, G.; Corticelli, F.; Morandi, V.; Zanelli, A.; Bellani, V.; Palermo, V. The exfoliation of graphene in liquids by electrochemical, chemical, and sonication-assisted techniques: A nanoscale study. *Adv. Funct. Mater.* **2013**, *23*, 4684–4693. [CrossRef]
114. Gregg, S.J.; Sing, K.S.W. *Adsorption, Surface Area and Porosity*; Academic Press: London, UK; New York, NY, USA, 1982.
115. Eller, K.; Henkes, E.; Rossbacher, R.; Höke, H. *Amines, Aliphatic. Ullmann's Encyclopedia of Industrial Chemistry*; Wiley-VCH Verlag GmbH & Co. KGaA: Weinheim, Germany, 2015.
116. Kanzow, J.; Zaporojtchenko, V.; Nabika, H.; Mizuhata, M.; Deki, S.; Faupel, F. In situ investigations on the cross-linking process of the epoxy resin system DGEBA-DETA by means of positron annihilation lifetime spectroscopy in comparison with infrared spectroscopy. In Proceedings of the 13th International Conference on Positron Annihilation, Kyoto, Japan, 7–12 September 2003; Nalwa, H.S., Ed.; Materials Science Forum. Trans Tech Publications: Zurich, Switzerland, 2004; Volumes 445–446, pp. 313–331. [CrossRef]
117. Moongraksathum, B.B.; Shang, J.-Y.; Chen, Y.-W. Photocatalytic antibacterial effectiveness of Cu-doped TiO_2 thin film prepared via the peroxo sol-gel method. *Catalysts* **2018**, *8*, 352. [CrossRef]
118. *ASTM C177-19*; Standard Test Method for Steady-State Heat Flux Measurements and Thermal Transmission Properties by Means of the Guarded-Hot-Plate Apparatus. ASTM International: West Conshohocken, PA, USA, 2019. [CrossRef]
119. *ASTM C1045-07*; Standard Practice for Calculating Thermal Transmission Properties Under Steady-State Conditions. ASTM International: West Conshohocken, PA, USA, 2013. [CrossRef]
120. Rondeaux, F.; Bredy, P.; Rey, J.M. Thermal conductivity measurements of epoxy systems at low temperature. *AIP Conf. Proc.* **2002**, *614*, 197–203. [CrossRef]
121. Physical Constants of IC Package Materials, Intel 2000 Packaging Databook. Available online: https://www.intel.com/content/dam/www/public/us/en/documents/packaging-databooks/packaging-chapter-05-databook.pdf (accessed on 24 October 2023).
122. Soltani, A. Equations of Spheroid and Ellipsoid Surface Area by Analytical Method. Cambridge Open Engage. 2022. Available online: https://www.cambridge.org/engage/coe/article-details/61f7a44963acba4ce3201236 (accessed on 24 October 2023).
123. Chang, S.-W.; Nair, A.K.; Buehler, M.J. Geometry and temperature effects of the interfacial thermal conductance in copper– and nickel–graphene nanocomposites. *J. Phys. Cond. Matter* **2012**, *24*, 245301. [CrossRef]

Disclaimer/Publisher's Note: The statements, opinions and data contained in all publications are solely those of the individual author(s) and contributor(s) and not of MDPI and/or the editor(s). MDPI and/or the editor(s) disclaim responsibility for any injury to people or property resulting from any ideas, methods, instructions or products referred to in the content.